

# On the global relationship between polarimetric radio occultation ~~observable $\Delta\Phi$~~ differential phase shift and ice water content

Ramon Padullés<sup>1,2</sup>, Estel Cardellach<sup>1,2</sup>, and F. Joseph Turk<sup>3</sup>

<sup>1</sup>Institut de Ciències de l'Espai, Consejo Superior de Investigaciones Científicas (ICE-CSIC), Barcelona, Spain

<sup>2</sup>Institut d'Estudis Espacials de Catalunya (IEEC), Barcelona, Spain

<sup>3</sup>Jet Propulsion Laboratory, California Institute of Technology, Pasadena, CA, USA

**Correspondence:** Ramon Padullés (padulles@ice.csic.es)

**Abstract.** The Radio Occultations and Heavy Precipitation (ROHP) experiment aboard the Spanish PAZ satellite was deployed in 2018 with the objective of demonstrating the ability of Polarimetric Radio Occultation measurement (PRO) concept in detecting rain (liquid-phase precipitation). Analysis of these data ~~since that time have~~ has also demonstrated the ability of PRO ~~for detection of~~ to detect horizontally oriented frozen-phase precipitation. To verify these observations, a global climatological comparison is performed using the Cloudsat (94-GHz) radar as a reference, for different heights and taking into account the radio occultation (limb-based) viewing geometry. A robust relationship (e.g. high correlation coefficient) is found between the polarimetric radio occultation observable differential phase shift ( $\Delta\Phi$ ) and the integrated ice water content along the rays for heights above the freezing level. The relationship is ~~especially good over ocean, where the~~ especially good over ocean, where major precipitation features and the signatures of the Inter-Tropical Convergence Zone are well captured by the PAZ observations. ~~Differences between over ocean and over land point towards different characteristics of the convective clouds above the freezing level, involving the orientation of frozen particles.~~ The ratios between  $\Delta\Phi$  and along-ray integrated ice water content are further ~~validated~~ evaluated with single particle forward scattering simulations, and the results indicate that the scattering by frozen hydrometeors with a combination of ~~horizontally oriented aggregated ice particles and tilted pristine ice plates~~ effective densities, axis ratios and tilt angle distribution yield results that agree well with the observations. Overall, the global climatological results obtained in this study show the presence of horizontally oriented particles across the whole globe, and for a wide range of height layers. ~~Furthermore, the relationship between  $\Delta\Phi$  and along-ray integrated ice water content can be used to attempt an inversion of the polarimetric radio occultation observations towards a potential retrieval of such water content.~~

## 1 Introduction

~~The National Academies' 2017 Decadal Survey for Earth Science and Applications from Space (National Academies of Sciences Engineering recommended an observing system that addresses the Aerosols, Clouds, Convection, and Precipitation (ACCP) combined designated observable, currently being formulated as the National Aeronautics and Space Administration (NASA) Atmosphere Observing System (AOS, part of the NASA Earth System Observatory) for later in this decade. The observations from the AOS instruments will be complemented by a program of record (POR) for geophysical variables (GV) that are not available at the~~

25 ~~time-of AOS, including ice-water-path measurements being envisioned as part of the primary GV of interest related to ice-phase clouds and precipitation.~~

~~A challenging GV to measure is the precipitation and ice profile properties directly inside, and to lower levels of convective clouds, where observations from radars that operate at attenuating wavelengths are compromised owing to multiple scattering and severe attenuation (Battaglia et al., 2020). While the convective cloud-vertical column is driven largely by the intensity and profile of moist convective up- and down-drafts, the convective vertical motions are controlled by exchanges between the local and regional thermodynamic environments in which convective clouds evolve (Schiro et al., 2018, 2020; Storer and Posselt, 2019). A joint profiling observation that provides an indication of convective strength alongside the thermodynamic profile may provide an observational constraint, such as representing the effects of entrainment of subsaturated air from the lower free troposphere to correctly capture the onset of convection.~~

35 The Radio Occultations and Heavy Precipitation (ROHP) experiment aboard the Spanish PAZ satellite (Cardellach et al., 2014) has demonstrated the ability of the polarimetric Radio Occultation (PRO) technique to complement well-established RO processing techniques (e.g. Kursinski et al., 1997) with a joint detection of heavy precipitation (Cardellach et al., 2019; Padullés et al., 2022). The detection is based on the total differential phase shift ( $\Delta\Phi$ ) accumulated along the RO ray paths, traveling from the Global Positioning System (GPS) satellite emitter to the dual linearly polarized (H, V) receiver on the PAZ Low Earth  
40 Orbiter (LEO). Being a limb-sounding technique, the rays travel through deeper layers of the atmosphere as the occultation advances, penetrating into the layers where clouds and precipitation are expected. The  $\Delta\Phi$  is measured in mm and is obtained by comparing the electromagnetic phase at both antenna ports (e.g.  $\Delta\Phi = \Phi_H - \Phi_V$ ), assuming that the phase measurements have been previously translated to optical length by the factor  $\frac{\lambda}{2\pi}$ . This differential polarimetric phase measurement, in units of length, is set as the primary observable for PRO. It depends on the hydrometeors encountered along the rays as follows  
45 (Cardellach et al., 2014):

$$\Delta\Phi = \int_L K_{dp} dL \quad (1)$$

where  $K_{dp}$  is the differential phase shift (mm/km) and  $L$  is the traveled distance (in km). The  $K_{dp}$  is defined as:

$$K_{dp} = 10^3 \frac{\lambda^2}{2\pi} \int_D \Re\{S_{hh} - S_{vv}\} N(D) dD \quad (2)$$

where  $\lambda$  is the wavelength (i.e. in the case of L-band GPS signals,  $\lambda = 0.192$  m, corresponding to 1.575 GHz),  $S_{hh, vv}$  are the  
50 co-polar components of the scattering amplitude matrix (m), and  $N(D)$  is the particle size distribution ( $m^{-4}$ ) as a function of the equivalent particle diameter,  $D$  (m).

$K_{dp}$  contains the dependence of PRO observable on a series of microphysics parameters, such as the size, the shape and the amount of hydrometeors. The scattering amplitude matrix ( $\mathbf{S}$ ,  $2 \times 2$ ) provides information of the scattered field after propagating through an ensemble of hydrometeors. It depends on the shape and type of the hydrometeors (e.g. raindrops, pristine ice

55 crystals, aggregate of ice particles, etc.). The dependence on the shape is often expressed in terms of the axis ratio, i.e. the ratio between the two main axis of the particle. For a perfectly spherical particle,  $S_{hh} - S_{vv} = 0$ . ~~It~~  $K_{dp}$  also depends on the size of the hydrometeors (generally directly linked to the shape and type). This dependence on the size is proportional to its volume, and therefore it is ~~proportional to~~ affected by the third moment of the  $N(D)$ . ~~While polarimetric RO do not provide any information on dynamics, the expanding data record provided by ROHP, to directly sense convective ice cloud properties jointly with the thermodynamic profile, provides a potentially unique addition to the POR.~~

The water content (WC) is also ~~proportional to~~ affected by the third moment of  $N(D)$  as (e.g. Bringi and Chandrasekar, 2001):

$$WC = \frac{10^{-3} \pi}{6} \rho_{w,i} \int_D D^3 N(D) dD \quad (3)$$

where  $\rho_{w,i}$  is the density ~~in  $\text{g cm}^{-3}$  and WC is expressed in  $\text{g m}^{-3}$ , typically of water or ice.~~ Therefore, it is expected that there exists a relationship between  $K_{dp}$  and WC. In fact, the use of  $K_{dp}$  to retrieve WC has been attempted before, for rain (e.g. Jameson, 1985) and for ice (e.g. Vivekanandan et al., 1994; Ryzhkov et al., 1998; Bukovčić et al., 2018) (e.g. Vivekanandan et al., 1994; Ryzhkov using radar at different frequencies ranging from S to K bands. However, in the case of ice and snow, there are additional factors that must be taken into account, namely, the percentage of horizontally oriented particles with respect to those that are randomly oriented, and the associated composition (i.e., dielectric constant of the ice/air media). In the case that all particles were randomly oriented, the  $K_{dp}$  would cancel out regardless of the amount of WC.

Shape and orientation of ice particles have a direct relationship with the life-cycle of precipitation (e.g. Gong et al., 2020). Furthermore, its knowledge is crucial for space-based retrievals of, for example, total ice water paths (e.g. Kaur et al., 2022) and could help in the assimilation of passive microwave data in the all-sky assimilation schemes (e.g. Barlakas et al., 2021). In this regard, PRO observations have potential to help constraining the orientation of the hydrometeors globally, with high vertical resolution. Other limb-sounding techniques, such as the Microwave Limb Sounder (MLS), have previously been used to sense ice particles (e.g. Wu et al., 2009) and constrain its orientation (e.g. Davis et al., 2005), but their vertical resolution is low.

In Padullés et al. (2022), the authors showed that the presence of horizontally oriented frozen particles is required in order to explain some of the PAZ PRO observations. In this new paper, we carry out an extensive analysis of the global relationships between water content and  $\Delta\Phi$ . To do so, a synthetic radio occultation mission is simulated based on ice water properties provided by the Cloudsat data products between 2006-2016. That is, a set of actual radio occultation rays are artificially placed overlaying the Cloudsat curtain-like observations, continuously thorough the whole period. In this way the Cloudsat observations, like radar reflectivity, and its retrievals, like ice water content (IWC), can be analyzed as if they were observed in RO geometry. The statistics gathered from these observations would be equivalent to any other RO mission, if this was able to measure such quantities.

This strategy arises from the fact that there are no coincident observations between the Cloudsat and PAZ, due to different orbit parameters. However, the artificially generated products enable us to compare, in a statistical or climatological way, the PAZ  $\Delta\Phi$  observations with ~~measurements and~~ retrievals from Cloudsat, such as the IWC.

In this paper we focus on the spatial correlations between the IWC as would have been sensed by RO geometries in Cloudsat measured backgrounds and the  $\Delta\Phi$  from PAZ. If these two quantities are related, the spatial patterns should agree and the correlation should be high. This paper is therefore structured as follows: in Section 2 the artificial products based on Cloudsat retrievals and actual RO geometries are described. In Section 3 the correlations and relationship between the actual PAZ observations and the generated products are investigated. Finally, in Section 4, forward scattering simulations are used to validate and contextualize the relationships found in the previous section. The paper ends with a discussion on the findings.

## 95 2 Cloudsat retrievals projected to RO geometries

The Cloudsat satellite was launched in April 28, 2006, and ~~has been operating~~ was regularly providing observations until August, 2020. It orbits at an approximate height of 715 km in a polar orbit (inclination of 98.2 deg) with an equatorial crossing time of about 1:30 PM. It carries a Cloud Profiling Radar (CPR) operating at 94 GHz (W-band) aimed at observing and characterizing clouds (Stephens et al., 2008). Its high frequency radar is particularly good at sensing the frozen part of clouds and precipitation, whereas it has problems in penetrating to the lower altitudes in the deepest convective regions of precipitating systems (e.g. Battaglia et al., 2007). The parameters observed and ~~derived~~ retrieved from Cloudsat, of interest for this study, consist of the radar reflectivity ( $Z_e$ ) in the 2B-GEOPROF product (Marchand et al., 2008), the IWC retrievals from the DARDAR product (Delanoë and Hogan, 2010) version 3 (Cazenave et al., 2019), and the IWC and particle size distribution parameters ( $N_t$  and  $\sigma$ ) in the 2B-CWC-RO product (Austin et al., 2009). Auxiliary thermodynamic parameters such as temperature and humidity have been obtained from the European Centre for Medium-range Weather Forecasts (ECMWF) model ~~in the ECMWF-AUX products,~~ provided along the IWC retrievals. All these parameters are obtained with a vertical resolution of 240 m from the surface up to 25-30 km. Since the aim of this study is the comparison with the PRO observations from PAZ, these parameters are transformed to the "RO observing frame", as is defined below.

In brief, radio occultation observations consist of a Low Earth Orbiter (LEO) tracking a Global Navigation Satellite System (GNSS) emitted signal while it is occulting behind the Earth horizon (e.g. Kursinski et al., 1997; Hajj et al., 2002). This results in the electromagnetic waves from GNSS crossing the different layers of the atmosphere ~~in a tangential way (tangentially~~ with respect to Earth's surface), what is commonly known as a limb sounding observation. One implication of this kind of measurement is that rays cross a long portion of the atmosphere, becoming longer as rays approach the surface. In fact, when rays penetrate below 20 km (region where clouds are expected), their traveled distance can be as large as  $\sim 800$  km. In the particular case of PRO, this has been discussed in Turk et al. (2021). Therefore, direct comparisons between the nadir-looking radar obtained parameters with measurements from RO does not provide relevant information in terms of understanding PRO observations.

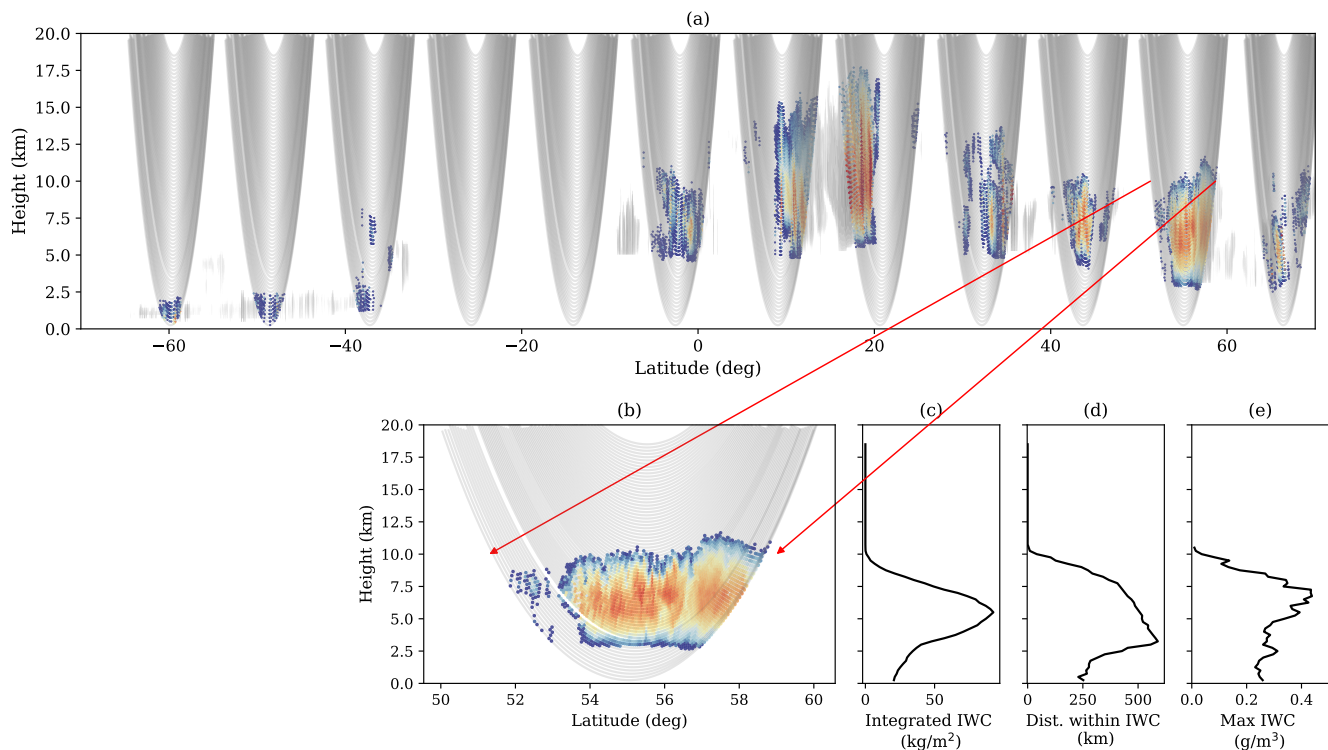


**Figure 1.** Example of half Cloudsat orbit observations (in this case, derived ice water content) with the RO rays overlapped. The Cloudsat orbit granule is 01075. In panel (a), only the Cloudsat ice water content being overlapped by RO rays are colored. IWC not being overlapped by RO rays are in gray-scale. Panel (b) shows a more detailed image of the Cloudsat derived ice water content interpolated into the RO rays, corresponding to one of the slices shown in panel (a) - indicated by the red arrows. In panels (c), (d), and (e) there is shown the corresponding integrated ice water content, distance traveled by the ray within the influence of IWC, and the maximum IWC encountered along the ray, respectively, as a function of each ray tangent height.

The approach followed in this study has been to re-map the Cloudsat observed and ~~derived~~retrieved parameters into the RO geometry. This is accomplished by using a set of actual RO rays and move and rotate them in order to place them overlaid to the curtain-like Cloudsat observations. RO rays often suffer from a drift as the occultation advances (e.g. the collection of rays do not form a perfectly vertical plane) due to the relative movement of the GNSS satellite and the LEO. However, for this study, the RO rays are collapsed into the Cloudsat vertical plane. Each Cloudsat orbit is split into 1200 km segments (resulting in approximately 29 segments per orbit), and the RO rays are placed in the middle of each of these segments. After that, Cloudsat observed and derived parameters are interpolated into the RO rays. See Fig. 1-(a and b) for an example of the procedure.

This approach permits the consideration of two relevant things. The first ~~one~~ is that one can see the actual extent, and therefore the influence area, of the cloud structures as sensed by PRO. The second one is that the actual amount of water content along RO rays can be quantified (e.g. see panel c in Fig. 1). Therefore, the integrated ice water content along these RO

rays can be compared with the PAZ PRO  $\Delta\Phi$  observations. Each RO ray is identified by the height of its lowest point along the ray (i.e. height of what is called the "tangent point"), so the integrated quantities are expressed as function of such height.

130 Such an exercise is repeated for all Cloudsat orbits between ~~2006 and 2016~~2009 and 2013, resulting in ~~684,036-342,109~~ artificial RO observations. For each of these artificial ROs, the following parameters are stored:

- Location and UTC time of each artificial RO observation. The location is determined by the latitude and longitude of the tangent point that has an altitude of 5 km. The UTC time is the one corresponding to the Cloudsat observation.
- ~~Minimum infra-red ( $11\mu\text{m}$ ) brightness temperature ( $T_{b_{11}}$ ) around a 1 deg radius from the location of the artificial RO, from the National Centers for Environmental Prediction Climate Prediction Center (NCEP CPC) geostationary satellites observations (Janowiak et al., 2017). This is stored because this quantity is routinely obtained for each PAZ PRO observation (Padullés et al., 2020), and it therefore provides a link between the two datasets.~~
- The integrated IWC ~~in  $\text{kg m}^{-2}$~~  (as a function of tangent height), and the maximum IWC ~~in  $\text{g m}^{-3}$~~  encountered along each ray (e.g. Fig. 1-(c and e)).
- 140 - The distance each ray traveled within the influence of non-zero water content, ~~in km~~ (e.g. Fig. 1-(d)).
- Additionally, vertical profiles of some thermodynamic parameters at the location of each artificial RO, like the temperature, pressure and specific humidity, are obtained from the ECMWF auxiliary files.

The resulting data are called hereafter the Cloudsat-RO database. ~~In addition to the aforementioned parameters, for a smaller portion of the Cloudsat mission corresponding to 2007,~~ Since the focus will be only on the IWC, each Cloudsat-RO event is truncated at the freezing level to avoid major contributions from liquid phase precipitation. For this study, the whole RO planes with the corresponding interpolated parameters are stored. These contain the Cloudsat observed  $Z_e$ , and the derived IWC and particle size distribution parameters  $N_r$  and  $\sigma$  effect of mixed-phase precipitation is not taken into account.

145

## 2.1 Statistics

Given that Cloudsat is orbiting on a polar orbit similar to that of PAZ satellite, and that ~~the used~~ RO rays are obtained from real RO events, the statistics gathered from the artificial collocation exercise should resemble the reality observed by PAZ. Furthermore, the integrated parameters along the RO rays mimic the behavior of  $\Delta\Phi$  observations, also obtained by PAZ as function of the tangent height. Therefore, ~~to analyze~~ analysis of the statistics of the artificial Cloudsat-ROs provides us with valuable information in order to understand the PAZ observations.

150

Figure 2 shows statistics of the along-ray integrated IWC, distance (here defined as the distance traveled by each ray within the influence of positive IWC), and maximum IWC encountered along each ray, obtained from the Cloudsat-RO database using the DARDAR product, corresponding to the rays whose tangent height is 9 km. The first thing to observe is the large values for the along-ray integrated IWC (e.g. Fig 2-d, with values up to  $250 \text{ kg m}^{-2}$ ), ~~compared with the typical values of vertical ice water path (e.g. Huang et al., 2015).~~ This is due to the long distances that rays travel through IWC. In this geometry, the

155

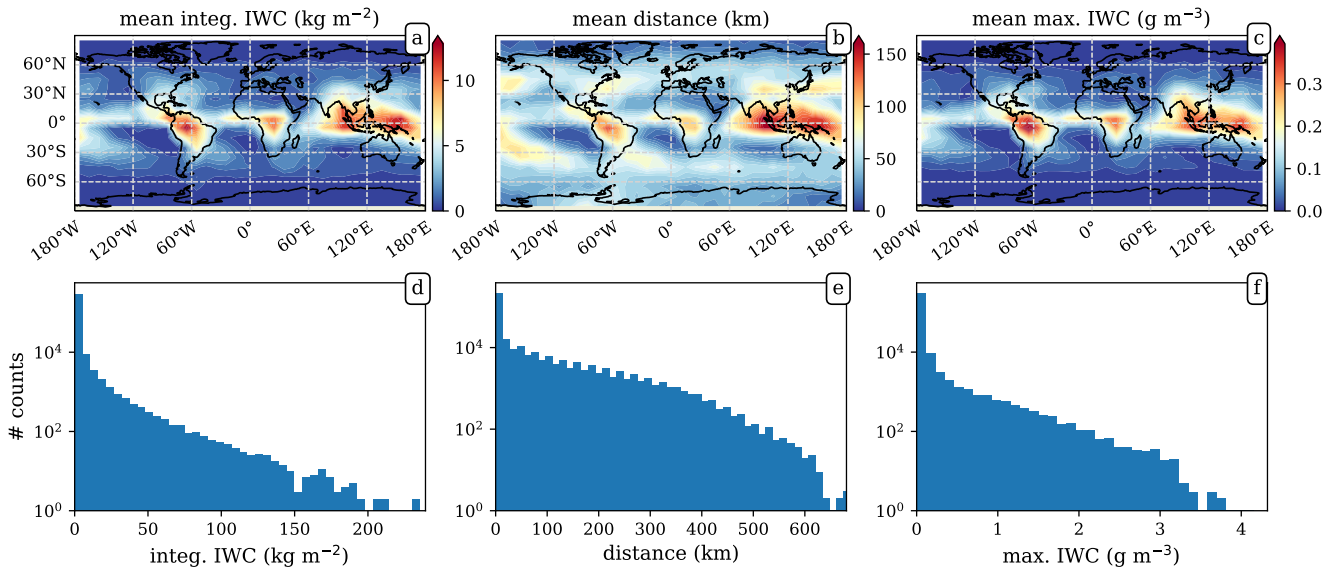


**Figure 2.** Statistics of the Cloudsat-RO database corresponding to the rays whose tangent height is 9 km. Panels (a), (b) and (c) show the mean value climatology for the along-ray integrated IWC, distance (i.e. distance traveled by each ray within the influence of positive IWC), and maximum IWC encountered along the ray, respectively. The used grid is  $10 \times 10$  deg. Panels (d), (e), and (f) correspond to the histograms for the total values for the same integrated IWC, distance, and maximum IWC as in the first row. [IWC source is the DARDAR retrieval product.](#)

distance relates more to the size of the storms being observed, as opposed to the vertical water path which relates stronger to their intensity. However, the broad range of distances (see Fig 2-e), reveals the ambiguity of PRO, ~~between the~~ [i.e. it cannot distinguish between the effects of](#) intensity of the storm (or amount of water content) and the distance within the influence of such water content (see Eq. 1).

~~Another relevant thing is the~~ [The](#) spatial/geographical patterns [are also relevant](#). Higher concentrations of IWC at 9 km occur in the tropics (as expected), specially over land (south America and central Africa) and around the West Pacific warm pool. Regarding the distance, large values also appear over the mid- and high- latitude oceans. This results agree well with known patters and previous characterization of storm features, such as in Liu and Zipser (2015), meaning that the RO geometry does not pose a problem in obtaining these global properties of heavy precipitation systems. Therefore, this database of IWC in RO geometry is well suited to both help understand the features observed in the PAZ  $\Delta\Phi$  and relate them to realistic precipitating systems.

[For this study, the DARDAR V3 retrieval has been used as a reference for the cross-comparison with  \$\Delta\Phi\$ . The choice has been made taking into account the assumptions in the IWC retrieval of both DARDAR and 2B-CWC-RO. DARDAR V3 has been recently improved with a lot of in-situ observations to help constrain the particle size distributions \(Cazenave et al., 2019\). A comparison between the integrated IWC from a Cloudsat-RO generated from DARDAR V3 and 2B-CWC-RO products is](#)

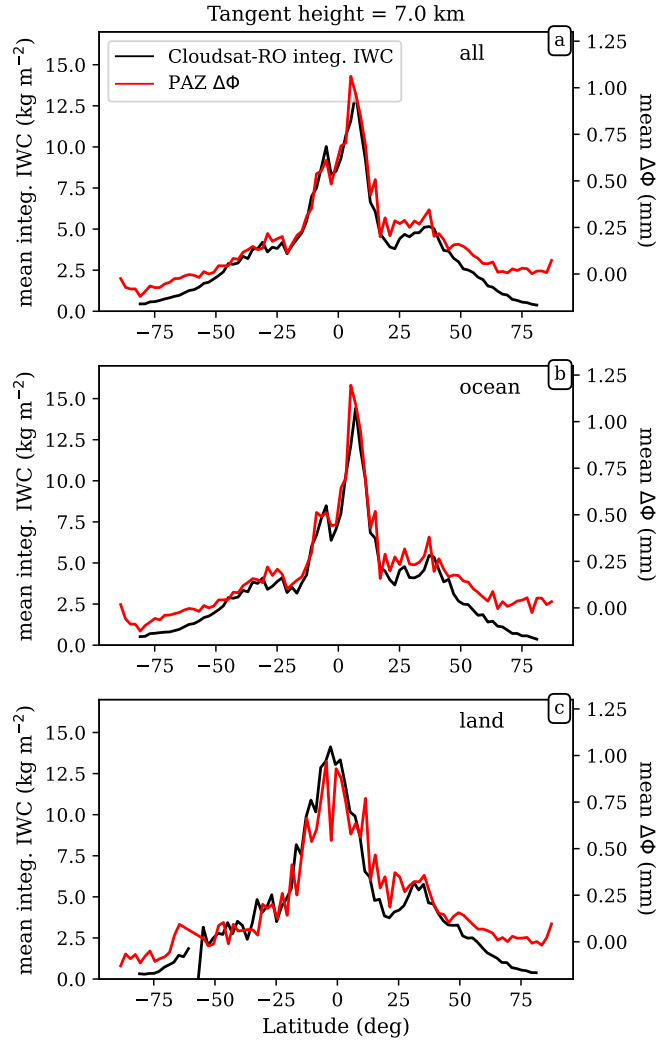


**Figure 3.** Mean values of integrated IWC (left axes) from the Cloudsat-RO dataset, and mean values of observed  $\Delta\Phi$  from PAZ (right axes), as a function of latitude, for all data (a), ocean (b) and land (c). Data correspond to tangent heights of 8 km. The mean values are computed for every 2 deg latitude bands.

[shown in Figure A1. The results shown hereafter will refer to those obtained using the Cloudsat-RO generated from DARDAR](#)

175 [V3.](#)

### 3 Relationship between PAZ $\Delta\Phi$ and Cloudsat [ice](#) water content

As it has been discussed in the introduction, both  $K_{dp}$  and WC [depend-on-are affected by](#) the third moment of the  $N(D)$ . Therefore, a relationship between the two is expected. Being the PRO observable,  $\Delta\Phi$ , an integral measurement, the corre-



sponding quantity to compare with would be the integrated WC along the same ray where  $\Delta\Phi$  has been measured. However, the  
180 PAZ satellite is in an 6AM/6PM orbit optimized for its primary sensor, which results in few crossover measurements with the  
GPM and CloudSat radars. Therefore, the comparison is performed ~~with the built~~ statistically with the Cloudsat-RO database ~~in~~  
~~statistical terms.~~

For the  $\Delta\Phi$  observations, the whole PAZ mission is used. That is, ~~152,319–189,487~~  $\Delta\Phi$  profiles between May 10th 2018  
and ~~November 30th 2021–~~ May 31th 2022. All these profiles have been selected so they have passed the initial quality controls  
185 and calibration (e.g. Padullés et al., 2020). PAZ  $\Delta\Phi$  data are available from <https://paz.ice.csic.es/>.

Figure 3 shows the comparison of the mean along-ray integrated IWC with the mean  $\Delta\Phi$ , as a function of latitude, corre-  
sponding to a tangent height of ~~8–7~~ 7 km. It can be seen how the two quantities agree remarkably well when the whole datasets  
are considered (panel a). The agreement is specially good over ocean (panel b). In the tropics, the shape of both the along-ray  
integrated IWC and  $\Delta\Phi$  capture very well the global precipitation signature of the Inter-Tropical Convergence Zone (ITCZ)  
190 (e.g. Marshall et al., 2014; Schneider et al., 2014). Over land (panel c), some features are still recognizable, but the general  
agreement is not as good as over ocean.

On a map, the gridded mean of  $\Delta\Phi$  can be seen in Figure 4. Panel (a) corresponds to the mean  $\Delta\Phi$  at a tangent height of 7 km,  
and panel (b) at a tangent height of 9 km. The latter can be compared with Fig. 2-a to investigate whether the spatial patterns  
are equivalent or not. In order to quantify the spatial relationship between the two (e.g. PAZ  $\Delta\Phi$  and Cloudsat-RO WC), the  
195 mean climatologies are computed on the same grid. The chosen grid is  $12 \times 12$  deg, so that spatial patterns of precipitation  
arise and there are enough PAZ observations to achieve significant statistics. The values for the mean ~~climatology of integrated~~  
~~Cloudsat-RO WC and~~ climatologies of PAZ  $\Delta\Phi$  and integrated Cloudsat-RO IWC obtained at the same grid cells are compared  
against each other (Figure 4-c). For the case of data corresponding to a tangent height of 9 km, the relationship follows a linear  
trend. The Pearson's correlation coefficient is ~~0.92–0.9~~ (e.g.  $r^2 = \del{0.86–0.81}) therefore exhibiting a robust relationship.$

200 The correlation coefficient for the spatial relationship between the mean PAZ  $\Delta\Phi$  and mean integrated Cloudsat-RO WC ~~and~~  
~~mean PAZ  $\Delta\Phi$~~  is computed for heights between 2 and 17 km. In addition to the mean, the climatologies for the 80th and 90th  
percentiles are also computed in order to check if the relationships stands at the higher ends of the distributions. The results are  
shown in Figure 5 (~~solid lines~~). Along with the correlation coefficient, the ratio between the ~~the mean integrated Cloudsat-RO~~  
~~WC and~~ mean PAZ  $\Delta\Phi$  and mean integrated Cloudsat-RO IWC is also computed ~~for all heights (dashed lines at the same~~  
205 heights and shown in Figure 5) ~~6~~. The values for the ~~two~~ first rows of ~~Figure 5~~ Figures 5 and 6 are summarized in Tables 1 and  
~~??~~ Table 1.

### 3.1 Correlations

The correlation coefficients in Figure 5 quantify the agreement between the spatial or geographical patterns of the two datasets.  
High correlations can be understood as the two datasets observing the same kind of precipitation structures. One thing to note  
210 before digging deeper into the results is that the correlation coefficient is computed assuming a linear relationship between the  
two quantities.

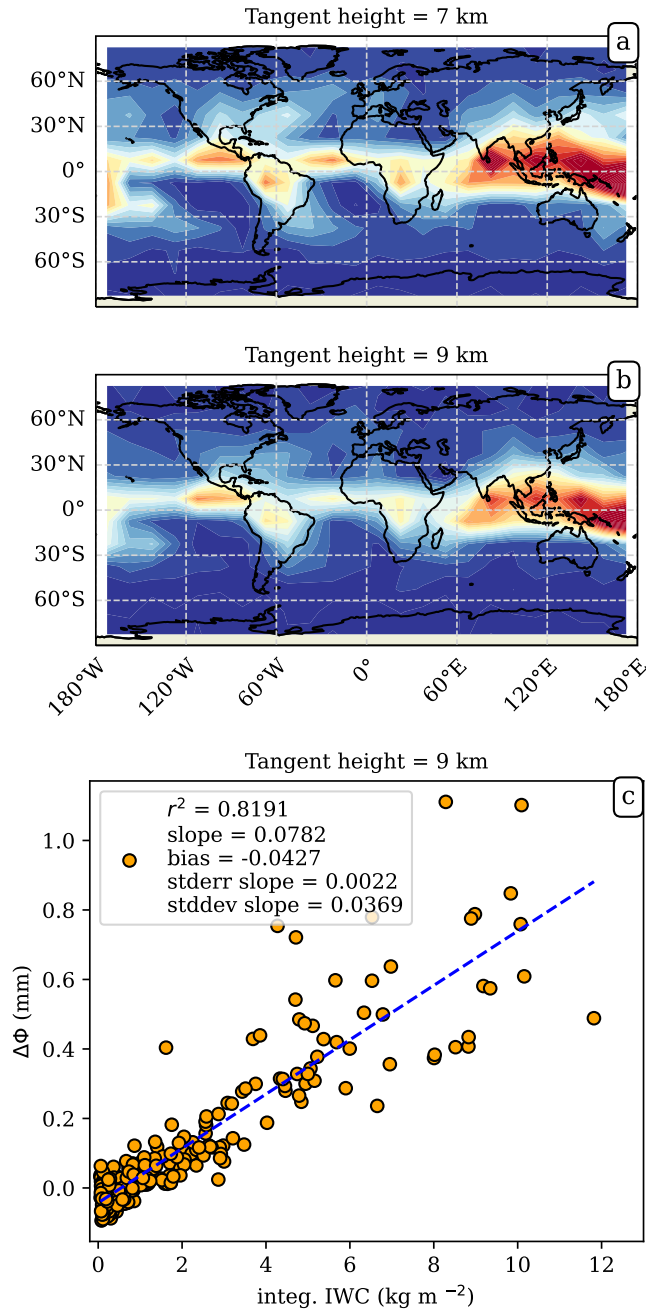


**Figure 4.** Global climatology maps for the mean PAZ  $\Delta\Phi$  observations corresponding to a tangent height of 7 km (panel a) and 9 km (panel b). The grid size where the means are computed is  $12 \times 12$  deg. Panel (c) shows the scatter plot of the mean climatologies of Cloudsat-RO integrated WC vs the PAZ  $\Delta\Phi$  obtained at the same grid cell, for the data corresponding to a tangent height of 9 km. Therefore, it is the comparison between panel (b) in this figure and Figure 2-a.

The results, in general (e.g. Figure 5, ~~a-e - first row~~, and Table 1 ~~-all data considered first column~~), show a very high correlation coefficient (i.e.  $\rho > 0.8$ ) ~~between 6 and 12 km. This among most of the considered heights. The correlation is particularly high over the oceans, although over land the agreement is also good. This is true for the three statistics being considered, the mean climatology, and the climatologies for the 80th and 90th percentile of the distributions. However, the correlation coefficient corresponding to the mean tends to be slightly higher than the other two.~~

When the data are split in different regions ~~and surfaces~~ (e.g. Figure 5, ~~d-mt tropics vs extra-tropics~~), more detailed features can be explored. The first relevant ~~thing is to observe one is the fact that~~ the correlation coefficient in the tropics (e.g. Figure 5, ~~d-f and Table ??~~), ~~which is high - second column) is higher~~ for a wider range of heights ~~, from 2 to 12-13 km. The correlation is specially high over ocean, with values exceeding 0.9 between 5 and 9 km. On the other hand, correlation coefficients over land are not as high as over ocean, although these exceed 0.7 from 2 to 10 km.~~

~~It is interesting to note the high correlation at heights expected to be below the freezing height (e.g. 2-5 km in the tropics). Due to the used geometry and retrievals (e.g. IWC from Cloudsat 2B-CWC-RO), it is expected that the ray-points below the freezing level are not contributed with ice water content (because it is liquid), meaning that the simulated integrated IWC from Cloudsat is basically contributed by the portion of the rays above freezing level. Then, than for the extra-tropical cases (Figure 5 - third and fourth columns). Also, it can be seen how for heights below  $\sim 4$  km, the correlation in the tropics drops due to the fact that the spatial correlation at the heights profiles have been truncated below the freezing level is high, indicates that the  $\Delta\Phi$  measurements at these regions are mostly contributed by the water content present in the frozen part of the cloud structures.~~

~~On the contrary, this behavior is not observed. The second relevant feature is that the correlation for the climatologies of the 80th and 90th percentiles are lower outside the tropics. For the regions corresponding to 70S-30S and 30N-70N (e.g. Figure 5, g-l) the correlation coefficient is very low below 5 km. It is worth noting that Finally, one must note that the panel corresponding to land in the southern hemisphere latitude range between 30-70S, cases over land are almost nonexistent. This explains the large dispersion in Figure 2-i panel. The low correlation coefficients in the southern oceans are further discussed in Sect. 5 (70S-30S) is contributed by a relatively small amount of data points, hence exhibiting a large dispersion of the correlation coefficients among different heights.~~

### 3.2 Ratios

~~For the regions and heights where~~

~~In addition of the correlation coefficient is high (bold numbers in Tables 1 and ??), the ratio between the Cloudsat-RO IWC and PAZ  $\Delta\Phi$  and Cloudsat-RO integrated IWC (i.e. ratio =  $IWC/\Delta\Phi$ ) provides empirical information on the  $IWC$  is computed for the same heights and regions as in Figure 5. Such a ratio provides an empirical relationship between the two quantities. In general, the ratio is low and it is shown in Figure 6. Furthermore, the uncertainty of such ratio (e.g. ratio  $< 10$ ) in the low layers (below 5 km), increases between 5 and 12 km, and decreases again for higher layers.~~

~~Unlike the correlation, the ratio between the IWC and  $\Delta\Phi$  is sensitive to all contribution to IWC. That is, in the lower layers where the contribution from liquid water content is missing in the Cloudsat-RO dataset, the ratio does not fairly represent the~~

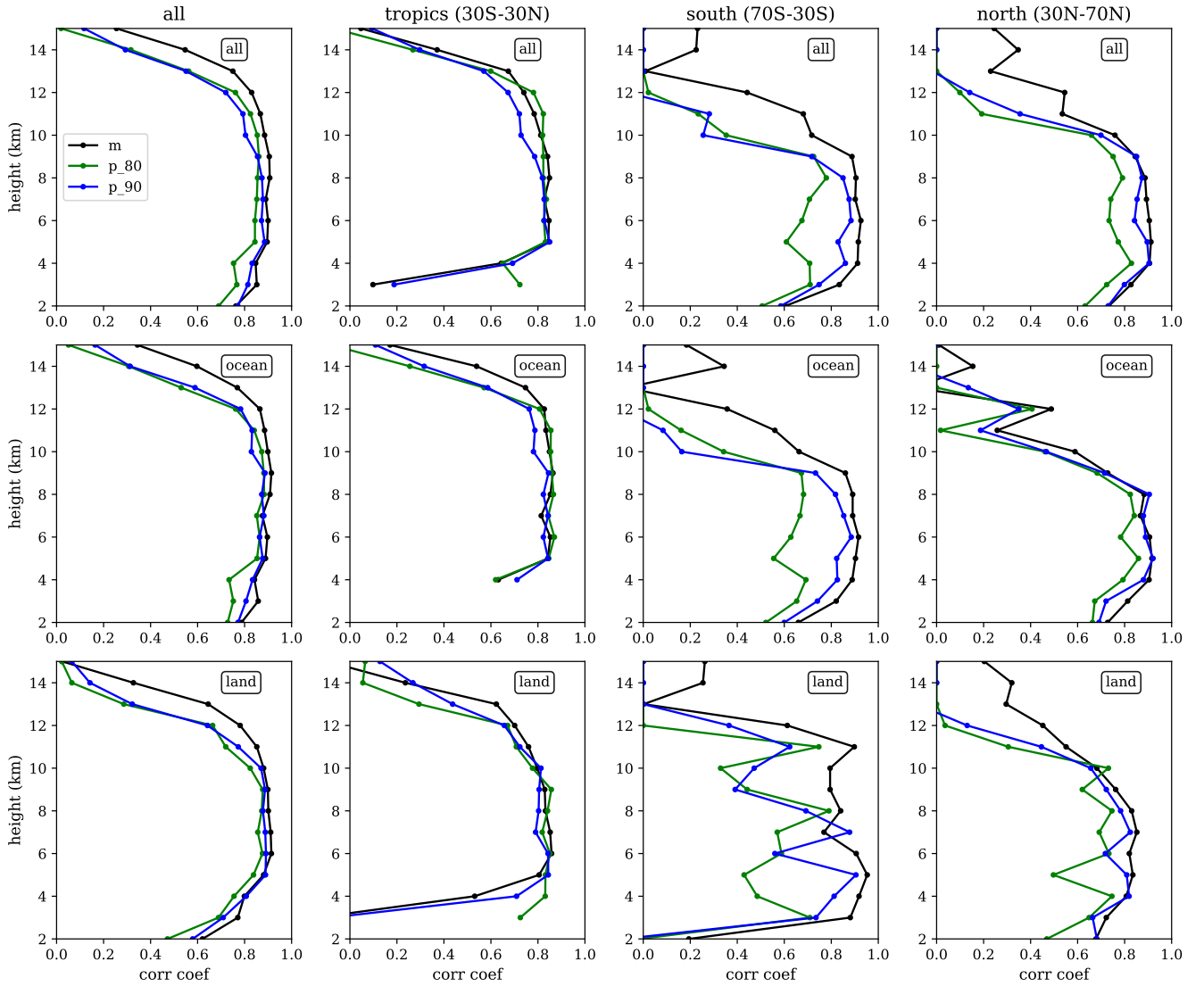


**Figure 5.** Correlation coefficients (solid lines—left axes) and ratio (dashed lines—right axes) between Cloudsat-RO IWC and PAZ  $\Delta\Phi$  and Cloudsat-RO IWC, as a function of height (x-axis-axis), for different areas across the globe (all globe, tropics, southern extra-tropics, and northern extra-tropics), and different surfaces (all, ocean, land). The black lines correspond to the mean climatologies, the green lines to the 80th percentile and the red lines to the 90th percentile climatology.

relationship between WC and  $\Delta\Phi$ . This effect could also appear in the uppermost layers, where Cloudsat high sensitivity might be accounting for more IWC than that contributing to  $\Delta\Phi$ . In addition, the ratio is highly sensitive to the % of horizontally oriented with respect to the amount of random-oriented frozen particles. This is further developed in Sect. 4 the standard

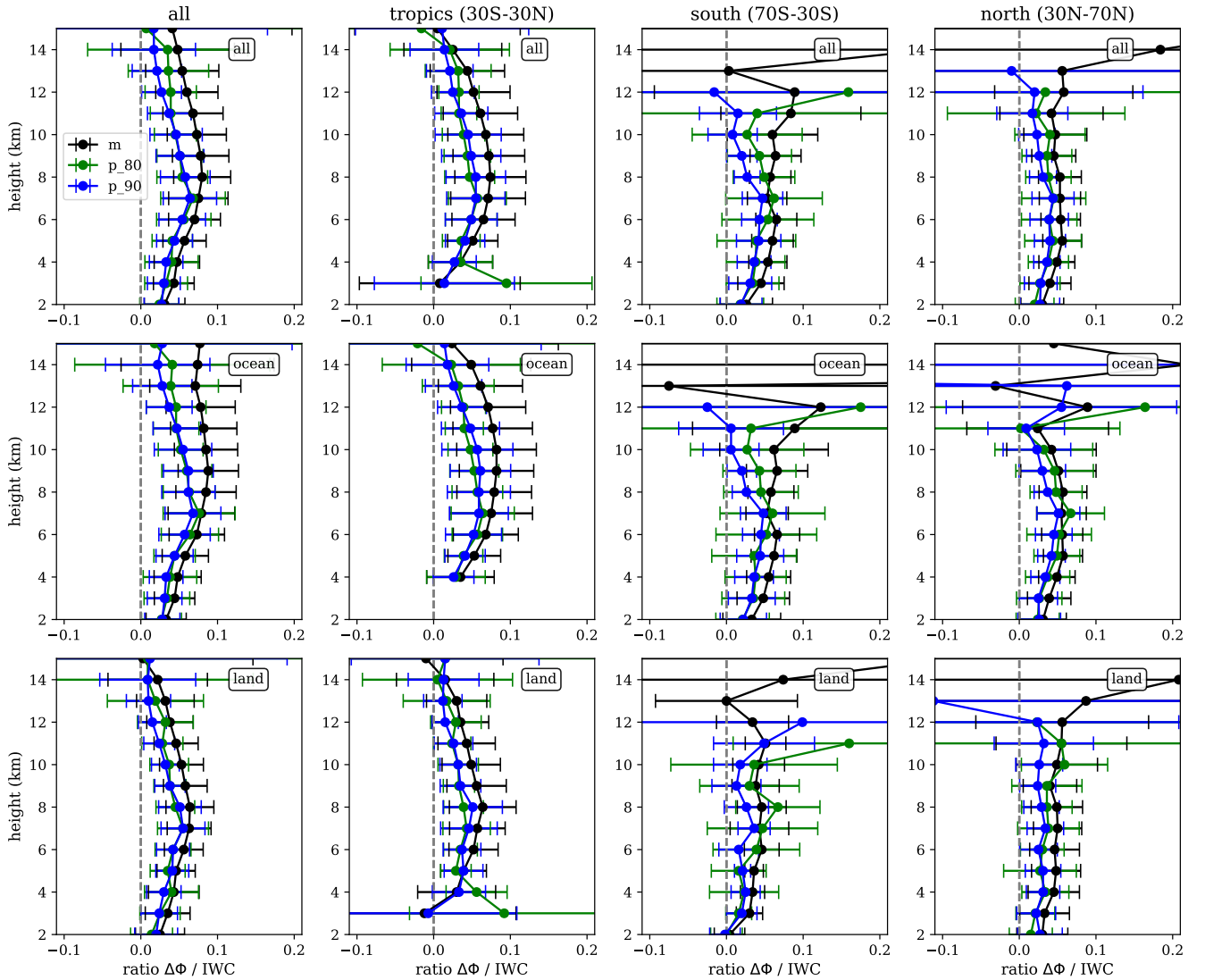


**Figure 6.** Ratio between PAZ  $\Delta\Phi$  and Cloudsat-RO IWC, as a function of height (y-axis), for different areas across the globe (all globe, tropics, southern extra-tropics, and northern extra-tropics), and different surfaces (all, ocean, land). The black lines correspond to the mean climatologies, the green lines to the 80th percentile and the red lines to the 90th percentile climatology. The x-axis errorbars show the standard deviation ( $1\sigma$ ) uncertainty around the mean ratio. The corresponding standard error is not shown, as it is one order of magnitude lower than  $\sigma$ .

250 deviation around the mean value) is obtained at each height when performing the linear fit between the climatologies (e.g. as shown in Figure 4-c).

**Table 1.** Values for the correlation coefficient and ratio between IWC and  $\Delta\Phi$  (top and bottom value in each cell, respectively), for different statistics (first column), different regions (second column) and different heights (first row). Data corresponds to the whole globe. Values in bold highlight correlation coefficients higher than 0.8.

height (km)		3	4	5	6	7	8	9	10	11	12	13	14
mean	all	<b>0.85</b> 0.043	<b>0.85</b> 0.047	<b>0.9</b> 0.057	<b>0.9</b> 0.07	<b>0.89</b> 0.075	<b>0.91</b> 0.08	<b>0.9</b> 0.078	<b>0.88</b> 0.073	<b>0.87</b> 0.068	<b>0.83</b> 0.06	0.75 0.054	0.55 0.048
	ocean	<b>0.86</b> 0.044	<b>0.84</b> 0.048	<b>0.89</b> 0.058	<b>0.9</b> 0.073	<b>0.88</b> 0.079	<b>0.91</b> 0.085	<b>0.91</b> 0.088	<b>0.9</b> 0.085	<b>0.88</b> 0.082	<b>0.86</b> 0.078	0.77 0.071	0.6 0.074
	land	0.77 0.035	0.8 0.043	<b>0.88</b> 0.046	<b>0.91</b> 0.056	<b>0.91</b> 0.063	<b>0.9</b> 0.064	<b>0.9</b> 0.058	<b>0.88</b> 0.053	<b>0.85</b> 0.046	0.78 0.038	0.64 0.032	0.33 0.022
p <sub>80</sub>	all	0.77 0.033	0.75 0.04	<b>0.84</b> 0.041	<b>0.84</b> 0.056	<b>0.85</b> 0.068	<b>0.86</b> 0.054	<b>0.86</b> 0.051	<b>0.85</b> 0.045	<b>0.82</b> 0.039	0.76 0.039	0.56 0.036	0.32 0.035
	ocean	0.75 0.034	0.73 0.038	<b>0.85</b> 0.044	<b>0.86</b> 0.064	<b>0.85</b> 0.076	<b>0.88</b> 0.063	<b>0.88</b> 0.06	<b>0.87</b> 0.052	<b>0.84</b> 0.046	0.76 0.046	0.53 0.039	0.31 0.041
	land	0.69 0.025	0.76 0.04	<b>0.84</b> 0.035	<b>0.88</b> 0.042	<b>0.86</b> 0.055	<b>0.87</b> 0.045	<b>0.88</b> 0.038	<b>0.82</b> 0.037	0.72 0.028	0.66 0.032	0.29 0.019	0.06 0.009
p <sub>90</sub>	all	<b>0.81</b> 0.03	<b>0.83</b> 0.033	<b>0.88</b> 0.044	<b>0.87</b> 0.054	<b>0.88</b> 0.064	<b>0.87</b> 0.058	<b>0.86</b> 0.051	<b>0.8</b> 0.046	0.79 0.037	0.72 0.027	0.55 0.021	0.29 0.017
	ocean	<b>0.81</b> 0.031	<b>0.83</b> 0.033	<b>0.88</b> 0.044	<b>0.86</b> 0.057	<b>0.88</b> 0.068	<b>0.87</b> 0.062	<b>0.89</b> 0.062	<b>0.83</b> 0.055	<b>0.83</b> 0.047	0.78 0.037	0.59 0.028	0.31 0.022
	land	0.71 0.024	<b>0.81</b> 0.03	<b>0.89</b> 0.041	<b>0.89</b> 0.042	<b>0.89</b> 0.055	<b>0.88</b> 0.051	<b>0.89</b> 0.038	<b>0.87</b> 0.032	0.77 0.024	0.64 0.015	0.32 0.01	0.14 0.009

Looking at the actual numbers and focusing only in those layers where the correlation coefficient is high (e.g. cc > 0.8). It can be seen how it has a trend with height and it exhibits differences at the different percentiles. In general, the ratio between the IWC and  $\Delta\Phi$  ranges between 5–20 for the mean climatological values tends to maximize at around 8/10km in the tropics, whereas the ratios reach values of around 25 outside tropics. It can also be seen that the ratio generally increase with height. At the higher ends of the distributions (e.g. and at a lower heights in the extra-tropics. Furthermore, the ratio corresponding to the 80th and 90th percentiles), the ratios are larger than for the means, but follow similar patterns percentile is smaller compared to the one corresponding to the mean climatology, in most heights and all regions.

### 3.3 Heavy precipitating cases and differences between ocean and land

#### 260 3.2.1 Results for a subset of heavy precipitating cases

To further examine the relationship between Cloudsat-RO WC and PAZ  $\Delta\Phi$ , in this section we focus on a subset of tropical (within  $\pm 30^\circ$  latitude) heavy precipitating cases. The cases (both the artificial RO and actual PAZ observations) where the  $Tb_{11} < 205\text{K}$  are selected. For the artificial cases, the 2-dimensional histogram (where y-axis is the height, and x-axis is the value being represented) of Cloudsat radar reflectivity, distance within the influence of non-zero water content, the IWC, and the two parameters  $N_r$  and  $\sigma$ , are shown in Figure ?? . These quantities correspond to those that have been integrated into the realistic RO plane (see Sect 2 for details). In addition, the mean and the 85th percentile of the integrated WC as a function of the tangent height for the selected cases are also shown. These results are further split in over ocean and over land cases (top and bottom rows). For the selected actual PAZ observations, the mean and the 85th percentile of the  $\Delta\Phi$  as a function of the tangent height are also shown, equally split in over ocean and over land. For representation purposes, the  $\Delta\Phi$  mean and 85th  
265 percentile are multiplied by a factor of 15.

In the results shown in Figure ?? two important things can be observed. First, that there is a clear difference between the  $\Delta\Phi$  observations over ocean and over land. While the mean integrated water content (and the corresponding 85th percentile) are relatively similar over ocean and over land (black and gray lines), there is a more obvious difference between the  $\Delta\Phi$  observations over ocean and over land. The fact that IWC is similar should lead to similar  $\Delta\Phi$ , but  $\Delta\Phi$  observed by PAZ tends to  
275 be diminished over land.

The second thing is that the  $\Delta\Phi$  and WC profiles over ocean agree well within each other and with the shape of the 2D histograms of radar reflectivity, distance within non-zero water content, and retrieved water content. The agreement is specially good above 6 km. Below that height,  $\Delta\Phi$  is probably being importantly contributed by liquid water content and therefore  $\Delta\Phi$  profile remains relatively higher than the cloudsat retrieved along-ray integrated IWC, which suffers an important drop in the  
280 lower layers.

The results over ocean confirms the robust relationship between the  $\Delta\Phi$  and the along-ray integrated IWC, even for the most extreme cases. The differences between ocean and land deserve a further discussion.

#### 3.2.1 Differences between ocean and land

Cloudsat measured and derived products shown in Figure ?? do not seem to be as different as to induce the large differences  
285 observed between the over ocean and over land  $\Delta\Phi$  profiles. This is further examined by plotting the cumulative distribution functions of these five same products for two fixed heights. This is shown in Figure ?? . Some differences are visible (e.g. larger reflectivity over land than over ocean, larger WC also over land) specially at 12 km. However, at 8 km these differences do not appear to be as significant, but the  $\Delta\Phi$  differences are.

These differences also reinforce the hints provided by the lower correlation coefficients (Sect. 3.1) that the relationship  
290 between  $\Delta\Phi$  and IWC over land is more complex than over ocean. The hypotheses for this complexity are developed in the discussion in Sect. 5.

Two dimensional histograms (being y-axis height, and x-axis the represented quantity) for the Cloudsat radar reflectivity ( $Z_e$ ) (a, f), the distance within the influence of non-zero water content (b, g), the Cloudsat retrieved IWC (c, h), the  $N_t$  parameter of the particle size distribution (PSD) (d, i) and the sigma parameter of the PSD (e, j) for the subset of cases where the  $Tb_{11} < 205$  K. The represented quantities correspond to those interpolated into the RO plane. Further details provided in Sect 2. The top row correspond to cases over ocean, and the bottom row to cases over land. Yellow (red-dashed) lines correspond to the mean (85th percentile)  $\Delta\Phi$  as a function of tangent height from the actual PAZ measurements—here following the top-axis and multiplied by a factor of 15. Black (dashed-gray) lines correspond to the mean (85th percentile) of the integrated IWC—following also the top-axis. The  $\Delta\Phi$  and WC vertical profiles are repeated in all panels (only differing over ocean vs over land).

Cumulative distribution functions for the quantities shown in Figure ??, for two fixed heights (12 km, first row; 8 km, second row) and for the cases over ocean (blue) and over land (orange).

#### 4 Forward scattering simulations of ice and snow

Results of the single particle forward scattering computations. (a) Difference between the co-polar components of the scattering amplitude matrix  $\mathbf{S}$  ( $S_{hh, vv}$ ) as a function of the equivalent melted diameter for a series of hydrometeors and ice particle habits (as indicated in the legend). For dry aggregates and wet snow, the first number indicates the effective density and the second one the axis ratio. See Sect. 4.1 for more details on the particles. (b)  $K_{dp}$  as a function of water content obtained using Eqs. 2 and 3 using common PSD obtained from one week of Cloudsat observations. For each type of particle, the mean ratio between WC and  $K_{dp}$  is shown in the right side of panel (b).

The correlation coefficients determined-obtained in Sect. 3.1 indicate a robust relationship between  $\Delta\Phi$  and IWC, specially integrated IWC, especially over tropical ocean. However, the meaning of the ratios between IWC and ratio between  $\Delta\Phi$  and integrated IWC depend on more factors. The aim of this section is to determine whether the ratios in Sect. 3.2 are physically meaningful or not. That is, to determine if the ratios are compatible with the characteristics of hydrometeors that are known to be present in clouds.

For this, the idea is to compute the  $K_{dp}$  - IWC relationship for a series of different hydrometeors and ice particle habits. This relationship can then be compared with the ratios in Fig. 5 and in Tables 1 and ??Figure 6 and in Table 1. To perform such comparison, first, the scattering amplitude matrix  $\mathbf{S}$  is computed for a set of different single hydrometeors and ice particle habits. Then, a set of particle size distributions from one week of Cloudsat observations are used to generate the corresponding  $K_{dp}$  and IWC using Eqs. 2 and 3. Note that for this study, only single particle scattering is considered.

##### 4.1 Hydrometeors and ice particle habits

The forward scattering simulations used for this study have been done using Rayleigh approximation. This formulation assumes that the particles can be approximated as oblate spheroids, with a certain axis ratio and effective density. The list of hydrometeors and ice particle habits that have been used are pristine ice crystals, aggregates of pristine ice, and wet snow. The



adequacy of using Rayleigh approximations is justified by the long wavelength of GNSS signals, i.e.  $\sim 190.3$  mm, much larger than the typical size of frozen hydrometeors. ~~However, for some pristine ice crystals and aggregates, a comparison using the Discrete Dipole Approximation (DDA, Draine and Flatau, 1994) has been performed.~~ For Rayleigh approximations, the formulations in Ryzhkov et al. (2011) and in Bringi and Chandrasekar (2001) have been followed. That is, the forward scattering amplitude co-polar components are computed using:

$$S_{hh,vv} = \frac{\pi^2 D^3}{6\lambda^2} \frac{1}{L_{hh,vv} + \frac{1}{\epsilon - 1}} \quad (4)$$

where  $\epsilon$  is the dielectric constant, and  $L_{hh,vv}$  are the shape parameters:

$$L_{hh} = \frac{1 + f^2}{f^2} \left( 1 - \frac{\arctan(f)}{f} \right), \quad f = \sqrt{\frac{1}{ar^2} - 1} \quad (5)$$

$$L_{vv} = \frac{1 + L_{hh}}{2} \quad (6)$$

where  $ar$  is the axis ratio of the particle. For the dielectric constant, the Maxwell-Garnett formula is used in order to account for the effective density of the particles as mixtures of ice, air, and water (Maxwell Garnett, 1904).

~~The results of the forward scattering simulations are shown in Fig. 7. The  $S_{hh} - S_{vv}$  as a function of the equivalent diameter for different types of frozen particles are shown in panel a, while the relationship of  $K_{dp}$  with water content for the same particles is shown in panel b. For some pristine ice crystals and aggregates, a comparison using the Discrete Dipole Approximation (DDA, Draine and Flatau, 1994) has been performed and compared with the Rayleigh results. The simulations have been performed using exact shape particles from Liu (2008), and the computation for aggregates follows the methodology in Leinonen and Moisseev (2015). The results (not shown) show good agreement with the Rayleigh approximations.~~

Below there are the specific details for each of the hydrometeors and habits used in this study.

#### 4.1.1 Pristine ice crystals

The simplest type of particles used in this study are pristine ice dendrites and thick plates. ~~For these, both the Rayleigh approximation and the exact DDA computations are performed. For the Rayleigh computation, the density of solid ice is used, and the values in Ryzhkov et al. (2011, Table 1) are used for the axis ratio. For the computation using DDA, exact shapes from Liu (2008) are used with the ADDA code (Yurkin and Hoekstra, 2011). For both methods, a fully horizontal orientation of the particles is assumed. The results using the Rayleigh approximation are shown in Fig. 7 (black squares-line for dendrites and cyan squares-line for the thick plates). The gray stars (ADDA results) on top of the Rayleigh results show the good agreement between the two methods for these kind of particles at L-band.~~

#### 4.1.2 Aggregates

For more complex shapes, we use aggregates of pristine ice particles. For the Rayleigh approximation, an spheroid of air filled with portions of ice is used, following Ryzhkov et al. (2011) and taking different values for the effective density and axis ratio.

The results are shown in Fig. 7, computation is performed for effective densities of 0.2, 0.5 and ranging from 0.1 to 0.9  $\text{g cm}^{-3}$ ,  
355 and axis ratios of ranging from 0.2 and 0.8 (an axis ratio of 1 would be a perfect sphere) to 0.9. Note that using an effective  
density of 0.9 means that the spheroid is filled with ice, approaching a pristine ice particle. The results using the Rayleigh  
method for fixed densities and fixed axis ratios for the whole range of equivalent diameters are called dry aggregates and are  
shown in Fig. 7 as star-lines.

For comparison purposes, exact computations of aggregates are also performed. To construct the shapes to be used with  
360 ADDA, the approach in Leinonen and Moisseev (2015) for dendrites and plates is followed. The only difference is that in this  
paper, the aggregate particles, once generated, are forced to lie in the most horizontally oriented plane as possible (i.e. the  
particles are rotated so that the longest dimension of the aggregated particle corresponds to the horizontal axis, and the shortest  
to the vertical). Like for the results in Sect. 4.1.1, the results obtained here with DDA are shown in Fig 7-a as gray stars, and  
these also fall on top of the solid lines representing the results of the Rayleigh approximation. In the comparison with the exact  
365 shapes, the Rayleigh approximation results are obtained by varying the density and axis ratio with the equivalent diameter,  
resembling the realistic shapes used for DDA (solid lines in Fig. 7).

### 4.1.3 Wet snow

Finally, wet snow aims to represent frozen particles at the initial stages of melting. For this, the same spheroids as in the  
previous subsection are used, but for this case a mass fraction of liquid water of a 10% of the total mass is used, in addition to  
370 pure ice and air, to compute  $\epsilon$ . The presence of water in the particle enhances  $\epsilon$  which in turn increases the  $K_{\text{dp}}$  with respect to  
the dry aggregates with same parameters (of equivalent density and  $ar$ ). For this case, only results for Rayleigh approximation  
are computed, and no exact computations have been performed.

The results are shown in Fig. 7 as triangle-lines for different values of effective density and axis ratio.

## 4.2 Orientation angle distribution

375 The results shown in Fig. 7-a corresponding to Sect. 4.1 for pristine ice, aggregates and wet snow are computed using single  
particle scattering and forcing the different particles to be horizontally oriented. For the exact computations using DDA, this is  
accomplished by placing the particle lying on the x-y plane on a x,y,z typical Cartesian plane (assuming an incident field in the  
y-direction), and averaging the results obtained by rotating the z-axis. The corresponding relationships between  $K_{\text{dp}}$  and WC  
shown in Fig. 7-b (square boxes over the right axis) are therefore for a collection of particles of the same type contributing to  
380 the whole water content and fully horizontally oriented. This is unlikely to be the case in real clouds and storms, and in fact,  
most of the ratios reported in Fig. 7-b are smaller than most of the observed ones (e.g. Fig. 5) and reported in Tables 1 and ??.

In real scenarios, where the orientation of these particles is more complex. To account for different orientation angles, we  
assume a Gaussian distribution of tilt (or canting) angles centered at  $0^\circ$  (hence mean angle  $\beta = 0^\circ$ ) with a certain standard  
deviation  $\sigma$ . This implies that varying  $\sigma$  we can range from total horizontal orientation ( $\sigma = 0^\circ$ ) to completely random orien-  
385 tation (large  $\sigma$ ). To keep the computations simple, we can use the horizontal orientation values and multiply them by a factor

that accounts for such canting (Oguchi, 1983):

$$K_{dp}^{\sigma} = \frac{1 + e^{-2\sigma^2} \cos(2\beta)}{2} e^{-2\sigma^2} K_{dp}^{\sigma=0} \quad (7)$$

The results for the different  $\sigma$  angles applied to the results of Fig. 7-b are shown in Table 2. The particle types have been sorted by the value of the ratio for  $\sigma = 0^\circ$ . For each

### 390 4.3 Simulations results

Using one week of Cloudsat retrieved  $N(D)$  at different heights above the freezing level, the IWC and  $K_{dp}$  are computed using the same particle type. This results in a set of  $K_{dp}$  vs IWC relationships for different hydrometeors or ice particle habits, and different properties such as effective density ( $\rho$ ) and axis ratios. In addition, for each combination of particle type, **computations using different  $\rho$  and  $ar$** , the corresponding result at different distributions of tilt angles are performed, **and the**. Figure 7 it is shown the variability of the  $K_{dp}$  vs IWC relationship, for dry aggregates (and wet snow), when one of the properties is varied (e.g. distribution of tilt angles -panel a-, effective density -panel b-, axis ratio -panel c-, and effective density for wet snow -panel d-).

The ratios between the  $K_{dp}$  and IWC for a subset of particles and different properties are shown in Table 2. The ratios with a value within the range [5-0.03 - 250.09] are highlighted in bold. These **values are the ones are the values** agreeing with the **observed values reported ratios between  $\Delta\Phi$  and integrated IWC** in Sect. 3(e.g. Fig. 5 and Tables 1 and ??).

In this results, it can be seen how for more pristine and thin particles, certain canting angle is required (e.g. fully horizontal orientation is overestimating the observed  $K_{dp}$ ), whereas for more complex particles, these are required to stay more horizontally oriented to better match the actual data. It can also be observed that very low density particles with high axis ratios (i.e. approaching empty spheres) alone cannot explain the observations.

To further validate observations and results obtained in Section 3 and allow for a more equivalent comparison between the results, a simple exercise is performed. It consists on computing the integrated IWC and  $\Delta\Phi$  using the simulations just described, and to proceed with the same procedure followed in Section 3 in order to obtain the same relationships. That is, to compute the mean climatological values at the same grid bins and heights, but in this case, for the simulated  $\Delta\Phi$  values. The obtained values for  $\Delta\Phi$  at all grid bins and heights are shown as a function of the corresponding integrated IWC at the same grid bins and heights in Figure 8 -top row-. This is done for dry aggregates with a different combination of  $\rho$  and  $ar$ , and for different tilt angles distribution. The same approach is used to compare the simulated  $\Delta\Phi$  with the observed one, as shown in Figure 8 -bottom row-.

These results are obtained assuming the same hydrometeor type at all heights for all situation, which is unrealistic. However, it can be used to explain the bulk of the observations, and further assess the effect of considering more or less tilted particles in the simulations in reproducing the observations. Comparing the simulated results with the observations (represented in the top row of Figure 8 as black dashed contour) it can be seen how the bulk observations can be reproduced dry aggregated particles, of a diverse effective density and axis ratio depending on how tilted they are (e.g., dry aggregate of  $\rho = 0.9 \text{ g cm}^{-3}$

**Table 2.** Ratio between  $K_{dp}$  and IWC for the different hydrometeors shown in Fig. 7, when a certain standard deviation is assumed in the orientation distribution (Gaussian distribution centered at  $0^\circ$  and  $\sigma$ )  $\sigma = 0^\circ$  represents the scenario where all particles are horizontally oriented, while for large  $\sigma$  all particles would be randomly oriented (see Eq. 7). In bold, the ratios within the range [0.03 - 0.09], in agreement with the observed ratios in Fig. 5 and Table 1.

	standard deviation of the Gaussian distribution of orientations, $\sigma$ ( $^\circ$ )								
	0	10	20	30	40	50	60	70	80
wet snow 0.9 ar 0.2	0.797	0.728	0.557	0.363	0.207	0.106	<b>0.049</b>	0.021	<0.015
crystal thick plate	0.607	0.555	0.424	0.277	0.158	<b>0.081</b>	<b>0.038</b>	0.016	<0.015
dry agg 0.9 ar 0.2	0.556	0.507	0.388	0.253	0.144	<b>0.074</b>	<b>0.034</b>	0.015	<0.015
wet snow 0.5 ar 0.2	0.414	0.378	0.289	0.189	0.108	<b>0.055</b>	0.026	<0.015	<0.015
agg plate	0.388	0.354	0.271	0.177	0.101	<b>0.052</b>	0.024	<0.015	<0.015
dry agg 0.5 ar 0.2	0.301	0.275	0.21	0.137	<b>0.078</b>	<b>0.04</b>	0.019	<0.015	<0.015
agg dendrite	0.288	0.263	0.201	0.131	<b>0.075</b>	<b>0.038</b>	0.018	<0.015	<0.015
crystal dendrite	0.216	0.197	0.151	0.098	<b>0.056</b>	0.029	<0.015	<0.015	<0.015
wet snow 0.9 ar 0.8	0.146	0.133	0.102	<b>0.067</b>	<b>0.038</b>	0.019	<0.015	<0.015	<0.015
wet snow 0.2 ar 0.2	0.131	0.12	0.092	<b>0.06</b>	<b>0.034</b>	0.017	<0.015	<0.015	<0.015
dry agg 0.2 ar 0.2	0.12	0.11	<b>0.084</b>	<b>0.055</b>	<b>0.031</b>	0.016	<0.015	<0.015	<0.015
dry agg 0.9 ar 0.8	0.103	0.094	<b>0.072</b>	<b>0.047</b>	0.027	<0.015	<0.015	<0.015	<0.015
wet snow 0.5 ar 0.8	<b>0.074</b>	<b>0.068</b>	<b>0.052</b>	<b>0.034</b>	0.019	<0.015	<0.015	<0.015	<0.015
dry agg 0.5 ar 0.8	<b>0.054</b>	<b>0.049</b>	<b>0.038</b>	0.025	<0.015	<0.015	<0.015	<0.015	<0.015
wet snow 0.2 ar 0.8	0.022	0.02	0.015	<0.015	<0.015	<0.015	<0.015	<0.015	<0.015
dry agg 0.2 ar 0.8	0.02	0.018	<0.015	<0.015	<0.015	<0.015	<0.015	<0.015	<0.015

and  $ar = 0.2$  must have a standard deviation of the tilted angle distribution larger than  $50^\circ$  in order to explain the observed relationships).

## 420 5 **Discussion Summary and Conclusions**discussion

### 5.1 Observations

The relationship between the PRO observable  $\Delta\Phi$  and ice water content has been investigated in a global and statistical (or climatological) way. For this purpose, ~~the measurements and~~ retrievals from the Cloudsat mission have been used. These have been re-mapped into the RO observation geometry so that comparisons take into account the important features of the observation geometry of PRO. An important one is the long distances that rays traveling from the GNSS satellites to the receivers in Low Earth Orbit spend in the lower layers of the troposphere. Such re-mapping allows an evaluation of the geometry

425

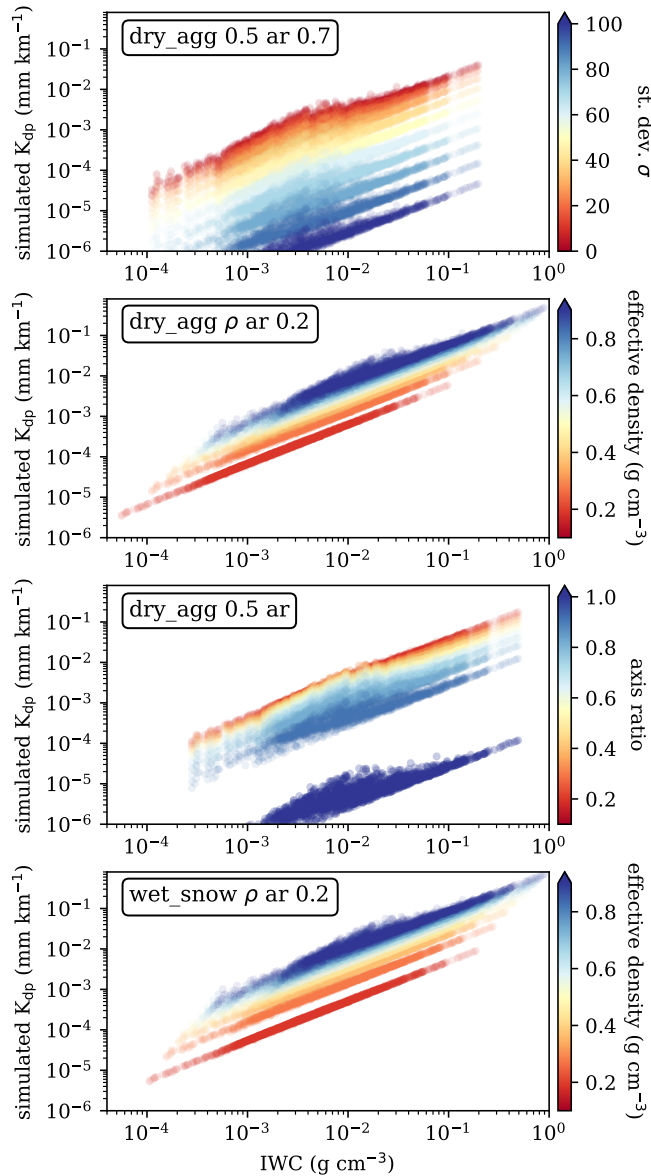


**Figure 7.** Results of simulated  $K_{dp}$  as a function of IWC for dry aggregates (a-b-c), and wet snow (d), varying the standard deviation of the tilt angle distribution (a), the effective density (b), axis ratio (c), and the effective density of wet snow (d).

itself. It can be assessed whether a limb-sounding measurement like PRO is able to capture important features of precipitation or not.

The results in Fig. 2 show the agreement between the climatology of the along-ray integrated ice water content (and related products such as the distance rays traveled within areas of non-zero ice water content, or the maximum ice water content

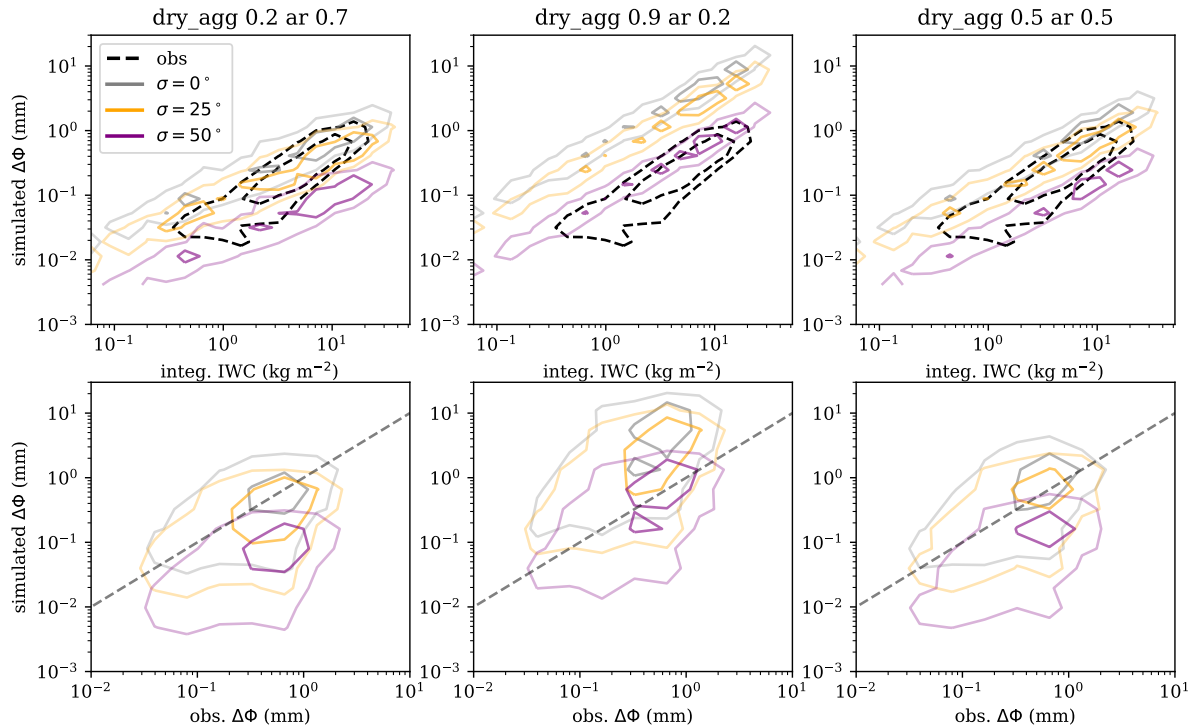


**Figure 8.** Results of the distributions of simulated  $\Delta\Phi$  vs integrated IWC (top row) and vs the observed  $\Delta\Phi$  (bottom row) compared at the same grid bins (same approach and same grid bins as in Figure 4) and accounting for all heights. Panel (a) and (d) show the results obtained using a single type of particle at all locations and heights - the dry aggregates with effective density of  $0.2 \text{ g cm}^{-3}$  and an axis ratio of 0.7. Panels (b) and (e) correspond to results using dry aggregates with effective density of  $0.9 \text{ g cm}^{-3}$  and an axis ratio of 0.2, and (c) and (f) using dry aggregates with effective density of  $0.5 \text{ g cm}^{-3}$  and an axis ratio of 0.5. The different colors of the contours correspond of different standard deviation in the distribution of tilt angles as described in the legend. The dashed contours (in the top row) correspond of the observed relationships as obtained in Sect. 3. The dashed line (in the bottom row) indicates the perfect 1:1 agreement. The same color inner and outer contours represent the contour containing 30% and 70% of the data, respectively.

encountered per ray) with known and previously studied heavy precipitation features (e.g. Liu and Zipser, 2015). This is further confirmed with the results in Fig. 3 (showing the mean climatology as function of latitude for water content, solid black line), which agrees very well with the signature of the ITCZ. Therefore, the good climatological agreement enables the use of the Cloudsat-based artificially collocated RO database of along-ray integrated ice water content for understanding the PRO  
 435 observations of precipitating cloud structures. For this study, only ice water content retrievals are used, and the profiles are truncated at the freezing level. The use of ice only retrievals is justified because Cloudsat observations in the liquid region of deep cloud structures (such as those specifically targeted by the ROHP experiment) may be degraded due to the high frequency and penetration issues. ~~However, the missing liquid part may have its implications, specially outside the tropics (as will be discussed below).~~

440 PRO observable  $\Delta\Phi$  is the integrated  $K_{dp}$  along each RO ray. Both  $K_{dp}$  and water content are ~~proportional to~~ affected  
by the third moment of the  $N(D)$ , and therefore a relationship between them is to be expected. ~~The~~ Such relationship is  
investigated by evaluating the correlation coefficient between the geographical patterns of the high and low concentrations of  
 $\Delta\Phi$  and along-ray integrated IWC, split in different regions and heights. Overall, correlation coefficients (e.g. Fig. 5) are high  
for the heights where frozen particles are expected (which changes by region, e.g. tropics vs. outside tropics). Tropical oceans  
445 is where the correlation coefficients maximize.

When the higher ends of the assumed distribution are evaluated (i.e. the 80th and 90th percentiles), similar behavior is  
observed. ~~When the results are inspected in more detail (detailed in Tables 1 and ??) differences are observed between the~~  
~~tropics and mid-latitudes, and between ocean and land. Tropical oceans is where the correlation coefficients maximize.~~

~~The main observed difference between tropics and mid-latitudes is the drop in the correlation coefficient for the lowest~~  
450 ~~heights. The difference in high altitudes is easily explained by the different maximum height of clouds, which is higher in the~~  
~~tropics. One important thing to take into account when focusing in the lower heights is that the ice water content retrieval from~~  
~~the Cloudsat mission is only applied in the frozen region (i.e. mostly above the freezing level). In the tropics, this level can~~  
~~be roughly approximated between 4-5 km. However, the correlation coefficient does not drop importantly below those heights~~  
~~(e.g. see the second row in Fig. 5). Since below the freezing height the contribution of liquid to the used integrated water~~  
455 ~~content is zero, the high correlation means that the contribution to the PRO  $\Delta\Phi$  in the areas that come from the frozen part of~~  
~~the rays is enough to reproduce the water content patterns. That is, the contribution of the liquid precipitation into  $\Delta\Phi$  does~~  
~~not seem to have an effect on changing the pattern of global features.~~

~~Large differences appear in the lower heights in the tropics, whereas differences between the mean climatology and the~~  
~~higher percentiles are observed in the mid-latitudes. It is of special concern the case of southern oceans (Fig. 5-h), where~~  
460 ~~the correlation coefficient drops significantly below 5 km, especially over the southern oceans.~~ This means that the features  
exhibited in the higher ends by the retrieved IWC in this region are not well captured by PAZ  $\Delta\Phi$  does not capture well the ice  
water content patterns from Cloudsat below these heights. It appears that PAZ  $\Delta\Phi$  largely underestimates the water content  
observed by Cloudsat. Therefore, this issue seems that would not be resolved by accounting for the liquid water content part.  
Mixed  $\Delta\Phi$ . One hypothesized explanation could relate to mixed phase clouds in the Southern Oceans (which are present in the  
465 lower heights ~~cloud tops reaching 3/4 km~~ in these areas), that have posed a longstanding issue for observations (e.g. Mace  
et al., 2021). Hence, further work must be carried out to assess whether the discrepancies between PAZ  $\Delta\Phi$  and Cloudsat  
Cloudsat-retrieved ice water content in these areas are due to microphysical reasons (e.g. smaller ice particles, lack of preferred  
orientation, etc.), observational errors, or still unaccounted factors.

~~Differences between observations over ocean and over land, specifically for the tropics, are further investigated and the~~  
470 ~~results are shown in Figures ?? and ??. The vertical distribution of microphysical quantities such as the cloudsat reflectivity,~~  
~~distance within the influence of ice water content, retrieved ice water content, and particle size distribution parameters are~~  
~~compared for a subset of cases where the associated infrared  $Tb_{11} < 205$  K. These correspond to heavily precipitating areas,~~  
~~and are further split between cases over ocean and over land. The same conditions are applied on the PAZ~~ The ratio between  
 $\Delta\Phi$  and Cloudsat-RO along-ray integrated ice water content aims at empirically relate both quantities. Results in Figure 6 and

475 Table 1 show the empirical relationship along with its uncertainty, at each height and for different regions. The uncertainties  
show the variation of the ratio around its mean and it shows how, even for mean climatological values, there is a dispersion  
that accounts for non-unique relationships between  $\Delta\Phi$  dataset, so that they can be compared. The first thing to notice is that  
the mean and integrated IWC. This could also be seen when comparing the ratios of the 85th percentile of the integrated  
480 ice water content (shown as a black and gray dashed lines on top of mean climatology with the ones corresponding to the  
histograms in Fig. ??) are similar for the cases over ocean and over land. Very small differences are noted if one focuses  
on the upper levels (where the mean IWC is slightly larger over land), which correspond to small differences pointing to the  
same direction in the vertical distribution of the microphysical quantities. However, the mean and 85th percentile of 80th and  
90th percentiles. The mean climatology ratio is higher. This is true for almost all heights and regions, and implies that the  
higher end of the distribution of IWC (e.g. regions with a larger concentration of IWC) relate differently to  $\Delta\Phi$  (shown as  
485 a orange solid and red dashed lines on top of the histograms in Fig. ??) are significantly different over ocean and over land.  
PRO  $\Delta\Phi$  is larger over ocean than over land for similar amounts of integrated ice water content. This difference is likely  
associated to differences in the microphysics, such as different frozen particles shapes, or preferred orientations. Differences in  
microphysical parameters of this kind are also observed in (e.g. Gong et al., 2018), where these are linked to the diurnal cycle  
variation, than the mean climatology.

490 In comparing PAZ with Cloudsat observations, we are comparing observations obtained at different local times. This is  
due to the difference in the equator crossing local times of the two satellite platforms (6AM This has been in fact observed in  
Gong and Wu (2017), where a decrease in the passive microwave polarimetric brightness temperature difference at 166GHz  
and 89Ghz is seen at very cold brightness temperatures, associated with very deep convective areas. An extreme example of  
such scenario applied here could be a region of large IWC with totally random oriented particles, where the ratio between  $\Delta\Phi$   
495 and IWC would tend to 0 despite having high IWC. This effect would be masked in the mean climatology, but could appear  
in individual observations. A more detailed study should be conducted to assess these situations, desirably with coincident  
observations between PRO and radars.

Another interesting feature of the ratio between  $\Delta\Phi$  and IWC shown in Figure 6 is that it is in general not constant with  
height. This could be associated to the presence of different particles at different heights, consistent with particle shape  
500 dependence on temperature and supersaturation (e.g. Bailey and Hallett, 2009). Furthermore, differences in the ratio trend  
with height can be observed between over-ocean and over-land, especially in the tropics, where a decrease in the correlation  
coefficient is observed at lower heights than for over-ocean. Two main hypothesis could explain the differences: (1) differences  
in the microphysics over-ocean and over-land, impacting the shape and orientation of the frozen particles; (2) differences owing  
to different local time observations between PAZ (6am/PM vs 9:30AM pm) and Cloudsat (1:30am/PM). While this could induce  
505 some discrepancies in the global comparisons (with pm). The latter would have stronger effect over land), for the subset of  
observations chosen for the Fig. ?? study, the effect of the diurnal cycle of precipitation is expected to be minimized, since  
the comparison is performed for storms that are already well developed. Therefore, the differences in microphysics (mostly  
orientation) must be related to the differences in physical processes taking place over ocean with respect to those happening  
over land. A dedicated study would be necessary to identify the causes, but a potential application of PRO in studies about



510 ~~microphysics is highlighted by the fact that these differences are detected.~~, but to discern between the two hypotheses more observations at different orbital planes are needed.

The ratio between the Cloudsat-RO along-ray integrated ice water content and  $\Delta\Phi$  aims at empirically relate both quantities. However, several considerations must be taken into account. Unlike with the correlation coefficient, here the lack of liquid contribution into the water content affects the result, since the ratio would be higher when liquid is considered. This would be true for the layers below 4-5 km, specially in the tropics, and therefore, conclusions must focus on the heights above freezing level. For these regions and where the correlation coefficient is high (i.e. bold values in Tables 1 and ??), the ratio provides an empirical estimate of the relationship between The robust relationships between PRO  $\Delta\Phi$  and integrated IWC has an implicit and important implication: it demonstrates the systematic presence of horizontally oriented frozen particles thorough the different vertical cloud layers (above freezing level), globally. This conclusion expands upon results in

515 Defer et al. (2014); Gong and Wu (2017); Zeng et al. (2019), where the presence of horizontally oriented particles was observed globally using the Microwave Analysis and Detection of Rain and Atmospheric Structures (MADRAS) instrument on board the Megha-Tropiques satellite and the Global Precipitation Mission Microwave Imager (GPM-GMI) polarization differences (PD) at 157, 89 and along-ray integrated ice water content. This is important for attempting a retrieval of such water content using PRO  $\Delta\Phi$ . 166 GHz. Thanks to the off-nadir looking instrument, the PD can be related to differential extinction by

520 asymmetric particles. Also, similarly as here with  $\Delta\Phi$ , using PD from passive microwave radiometers provide a single column measurement, but in the quasi-vertical direction. Here, however, we can include the vertical information lacking to off-nadir looking microwave measurements.

~~Single-~~

## 5.2 Simulations

530 Seeking to assess the feasibility of the results in Section 3, single particle forward scattering simulations have been used to assess whether the relationships obtained between ~~water content and~~  $\Delta\Phi$  and ice water content are reliable, according to the typical types of hydrometeors found in clouds. The ~~results shown in Fig 7~~and assumptions made for the simulations are quite simple, e.g. mostly focused on dry aggregates with a range of  $\rho$ ,  $ar$  and tilt angle distributions.

535 Using a subset of  $N(D)$  and the simulated  $S$ , the relationship between IWC and  $K_{dp}$  is shown in Figure 7, where a wide diversity of combinations of tilt angle distributions, effective densities and axis ratios is computed. Many different combinations yield similar results in the relationship  $K_{dp}$  vs IWC, revealing the large amount of degrees of freedom in ice particle forward scattering simulations.

The results of the ratio between  $K_{dp}$  and IWC for a subset of particles with some combinations of  $\rho$ ,  $ar$  and tilt angle distributions are summarized in Table 2. It is also compared with the results in Section 3.2. The comparison allow us to

540 corroborate that the observed ratios in the regions with high correlation coefficients ~~fit very well within the expected ranges.~~ Furthermore, can be explained with the simulations using simple approximations, and helps constraining the kind of particles that are likely to be contributing to IWC or not. For example, particles with large axis ratios (e.g. approaching spheres) cannot

reproduce the bulk of observed ratios between  $\Delta\Phi$  and IWC. Similarly, thin, solid ice particles would need to be oriented with a large dispersion in the tilt angle for the ratios to be consistent with observations.

545 Statistically comparing the simulated and observed  $\Delta\Phi$  and IWC relationship repeating the approach followed in Section 3 but using the simulated  $K_{dp}$  (Figure 8), a fairly good agreement is also reached with simple assumptions about the particles and changing the tilt angle distributions. However, the dispersion in Figure 8- bottom row, when comparing simulated with observed gridded mean  $\Delta\Phi$  is probably indicating that using the same particle assumptions for all regions and heights is not realistic. A better simulation exercise would be required, e.g. with Numerical Weather Prediction model outputs with  
550 detailed information about the hydrometeor species, to further constrain the valid particle shapes and tilt angle distributions that better match the observations (similarly to what is done in Brath et al. (2020)). However, and despite the simplicity, the results obtained here seem compatible with those by Brath et al. (2020). They showed how previously observed relationships between passive microwave brightness temperatures and its polarization differences could be explained accounting for tilted large snow thin plates, or less tilted more complex snow aggregates.

555 ~~The robust relationships between PRO  $\Delta\Phi$  and integrated ice water content has an implicit and important implication: it demonstrates the systematic presence of horizontally oriented frozen particles thorough the different vertical cloud layers (above freezing level~~ An important note to add is that the results presented here are valid for the chosen IWC retrieval algorithm (in this case, the DARDAR V3), and for all latitudes (with some caveats on the lower heights for mid- and high-latitudes). This conclusion expands upon results in Gong and Wu (2017); Zeng et al. (2019) are therefore dependent on that choice. As  
560 can be seen in Appendix A, differences between IWC retrieved in the 2B-CWC-RO product and DARDAR can be large at some heights. This results (not shown) in differences in the computed correlation coefficients at lower heights (i.e. near the freezing level), where the ~~presence of horizontally oriented particles was observed globally using the Global Precipitation Mission Microwave Imager (GPM-GMI) polarization differences at 89 and 166 GHz. However, here we include the vertical information lacking to off-nadir looking microwave measurements~~ results using DARDAR exhibit larger values for a wider  
565 range of heights for most regions. Some differences also appear in the values of the ratios. As a consequence, the combination of  $\rho$ ,  $ar$  and tilt angle distributions that explain the observed mean ratios would change, but for most regions and heights would remain within the expected values.

~~Furthermore, the consistency and similitude of the mean, 80th and 90th percentile profiles of IWC~~

## 6 Conclusions

570 This study assessed the global relationship between polarimetric radio occultation observable  $\Delta\Phi$  and ice water content retrieved by Cloudsat. First of all, the integrated IWC retrievals from Cloudsat have been re-mapped into the RO-like geometry. This has been used to demonstrate that RO-type limb-sounding observations can be used to sense and detect known precipitation features globally.

The global climatology of Cloudsat-retrieved integrated IWC has been compared to the  $\Delta\Phi$  climatology from PAZ. It has  
575 been shown how the spatial/ ~~$\Delta\phi$  (see Fig. 5) indicate little dispersion~~ geographical correlation between the two datasets is high

( $cc > 0.8$ ) for a wide range of heights, and especially good over tropical oceans. This means that the IWC concentration patterns are well captured by PRO observations, globally and at different heights.

580 ~~Analysis of the ratio values at each altitude, region and surface type (ocean/land). Therefore,  $\Delta\phi$  can be seen as a robust proxy for water content, enabling a simple way to invert the vertical profiles of polarimetric phase shift to vertical profile of integrated water content. At the current data volume rate of 250 RO/day, and assuming a 10-year life for ROHP, a data record of approx. 1 million ROHP observations will be available near the end of this decade. This number may be complemented by polarimetric RO observations collected by and/or for observational weather agencies between  $\Delta\Phi$  and the integrated IWC yields interesting results as well. First of all, the existence of such relationship between the both quantities implies the systematic presence of horizontally oriented hydrometeors contributing to IWC, globally and at all heights. Furthermore,~~  
585 ~~forward scattering simulations of simple snow aggregates accounting for a range of effective densities, axis ratios, and tilt angles distributions can explain the bulk of the ratios (i.e. the mean values). The simulation framework described here, although being very simple, can easily scale in complexity for arbitrary complex inputs of ice particle habits from, e.g. from Numerical Weather Prediction models.~~

590 ~~Despite the good agreement between the mean values of  $\Delta\Phi$  and integrated IWC, further work must be pursued to explore individual simultaneous observations of  $\Delta\Phi$  and IWC, and assess when and under which scenarios the relationship holds (i.e. horizontally oriented particles contribute to the IWC) or does not apply (i.e. mostly non oriented ice contributing to IWC). This is enabled by the fact that  $\Delta\Phi$  observations inherently provide unique information of the orientation of hydrometeors.~~

#### **Appendix A: Comparison between DARDAR and 2B-CWC-RO integrated IWC profiles**

595 ~~A comparison of the integrated IWC from the Cloudsat retrieval using the 2B-CWC-RO and DARDAR V3 products has been performed and is shown in Figure A1. The differences in general are shown in panel (a). A more detailed view of the DARDAR V3 - 2B-CWC-RO integrated IWC at different heights is shown in panel (b). The differences are positive (i.e. DARDAR V3 > 2B-CWC-RO) and larger at lower layers, and shift to negative (i.e. DARDAR V3 < 2B-CWC-RO) at upper layers. The differences arise from different assumptions regarding the treatment of the Cloudsat observations near the freezing level, the assumptions about the particle size distributions, and DARDAR includes Calipso observations to complement Cloudsat~~  
600 ~~observations (Delanoë and Hogan, 2008, 2010; Cazenave et al., 2019; Austin et al., 2009).~~

~~The differences in the integrated IWC change the results from Section 3. The correlation coefficient exhibit lower values for heights near the freezing level when 2B-CWC-RO is used. The ratios between the  $\Delta\Phi$  and the integrated IWC change accordingly to the differences between the two IWC product, since  $\Delta\Phi$  is the same.~~

605 *Data availability.* The datasets used for this work are the following: The PAZ polarimetric Radio Occultation data can be obtained from <https://paz.ice.csic.es> (last accessed: October 12, 2022). The DARDAR dataset can be obtained from <https://www.icare.univ-lille.fr/> (last

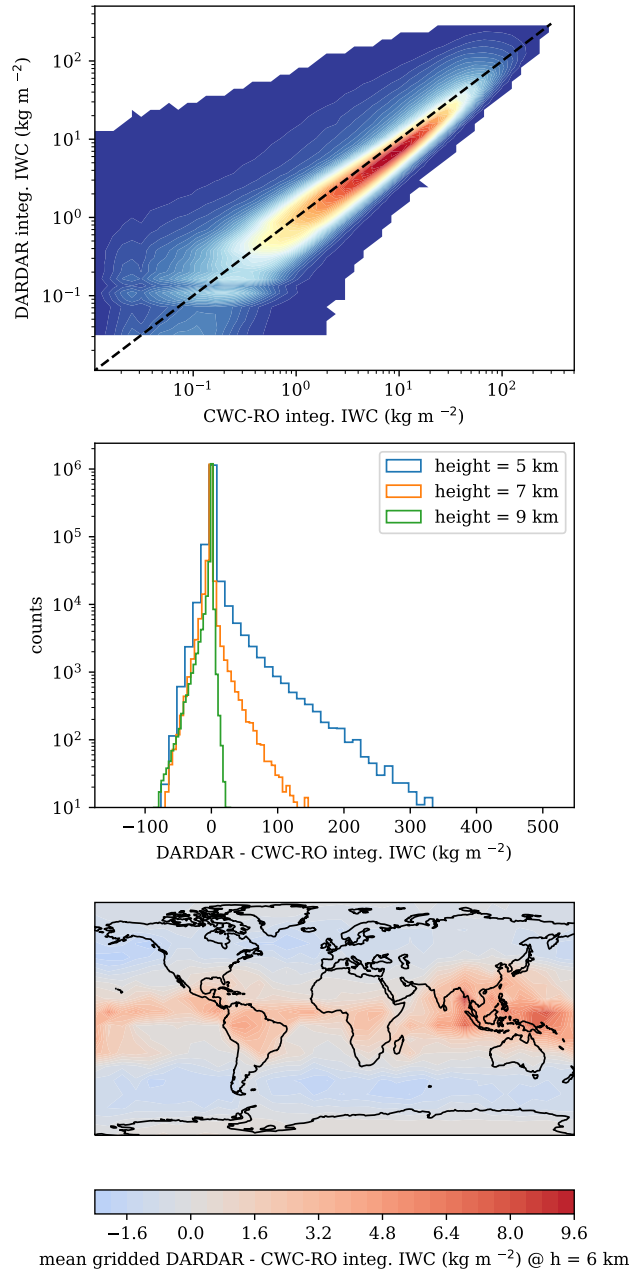


**Figure A1.** Comparison between the integrated IWC from the Cloudsat retrieval using the 2B-CWC-RO and DARDAR V3. Panel (a) shows the relationship between integrated IWC from the 2B-CWC-RO (x-axis) and DARDAR V3 (y-axis) for all observations regardless of height. Panel (b) shows the difference DARDAR V3 - 2B-CWC-RO integrated IWC corresponding to different tangent heights as detailed in the legend. Panel (c) shows the gridded mean DARDAR V3 - 2B-CWC-RO integrated IWC corresponding to a tangent height of 6 km.

accesses: October 12, 2022). The Cloudsat 2B-CWC-RO dataset can be obtained from <https://www.cloudsat.cira.colostate.edu/> (last accessed: October 12, 2022)

*Author contributions.* All co-authors have reviewed, discussed, and agreed to the final version of the manuscript. Conceptualization: RP, EC, FJT; Data analysis: RP; Investigation: RP, EC, FJT; Writing – original draft preparation: RP; Writing – review & editing: RP, EC, FJT;  
610 Funding acquisition: EC, FJT.

*Competing interests.* The authors declare no competing interests

*Acknowledgements.* [The authors would like to thank Patrick Eriksson and one anonymous reviewer for their comments and suggestions, which definitely help improve the paper.](#)

RP has received funding from the postdoctoral fellowships program Beatriu de Pinós, funded by the Secretary of Universities and Research  
615 (Government of Catalonia) and by the Horizon 2020 program of research and innovation of the European Union under the Marie Skłodowska-Curie grant agreement No 801370. This work was also partially supported by the program Unidad de Excelencia María de Maeztu CEX2020-001058-M. The ROHP-PAZ project is part of the Grant RTI2018-099008-B-C22 funded by the Spanish Ministry of Science and Innovation MCIN/AEI/10.13039/501100011033 and by “ERDF A way of making Europe” of the “European Union”. Part of the investigations are done under the EUMETSAT ROM SAF CDOP4. FJT acknowledges support from NASA under the US Participating Investigator (USPI) program.  
620 The work performed by FJT was conducted at the Jet Propulsion Laboratory, California Institute of Technology, under a contract with NASA.

## References

- Austin, R. T., Heymsfield, A. J., and Stephens, G. L.: Retrieval of ice cloud microphysical parameters using the CloudSat millimeter-wave radar and temperature, *Journal of Geophysical Research Atmospheres*, 114, 1–19, <https://doi.org/10.1029/2008JD010049>, 2009.
- Bailey, M. and Hallett, J.: A Comprehensive Habit Diagram for Atmospheric Ice Crystals: Confirmation from the Laboratory, AIRS II, and  
625 Other Field Studies, *Journal of Atmospheric Sciences*, 66, 2888–2899, <https://doi.org/10.1175/2009JAS2883.1>, 2009.
- Barlakas, V., Geer, A. J., and Eriksson, P.: Introducing hydrometeor orientation into all-sky microwave and submillimeter assimilation, *Atmospheric Measurement Techniques*, 14, 3427–3447, <https://doi.org/10.5194/amt-14-3427-2021>, 2021.
- Battaglia, A., Ajewole, M. O., and Simmer, C.: Evaluation of radar multiple scattering effects in Cloudsat configuration, *Atmospheric Chemistry and Physics*, 7, 1719–1730, <https://doi.org/10.5194/acp-7-1719-2007>, 2007.
- 630 Battaglia, A., Kollias, P., Dhillon, R., Roy, R., Tanelli, S., Lamer, K., Grecu, M., Lebsock, M., Watters, D., Mroz, K., Heymsfield, G. M., Li, L., and Furukawa, K.: Spaceborne Cloud and Precipitation Radars: Status, Challenges, and Ways Forward, *Reviews of Geophysics*, 58, 1–59, <https://doi.org/10.1029/2019RG000686>, 2020.
- Brath, M., Ekelund, R., Eriksson, P., Lemke, O., and Buehler, S. A.: Microwave and submillimeter wave scattering of oriented ice particles, *Atmospheric Measurement Techniques*, 13, 2309–2333, <https://doi.org/10.5194/amt-13-2309-2020>, 2020.
- 635 Bringi, V. N. and Chandrasekar, V.: *Polarimetric doppler weather radar; principles and applications*, Cambridge University Press, Cambridge, 2001.
- Bukovčić, P., Ryzhkov, A. V., Zrnić, D. S., and Zhang, G.: Polarimetric radar relations for quantification of snow based on disdrometer data, *Journal of Applied Meteorology and Climatology*, 57, 103–120, <https://doi.org/10.1175/JAMC-D-17-0090.1>, 2018.
- Cardellach, E., Tomás, S., Oliveras, S., Padullés, R., Rius, A., de la Torre-Juárez, M., Turk, F. J., Ao, C. O., Kursinski, E. R., Schreiner,  
640 W. S., Ector, D., and Cucurull, L.: Sensitivity of PAZ LEO Polarimetric GNSS Radio-Occultation Experiment to Precipitation Events, *IEEE Transactions on Geoscience and Remote Sensing*, 53, 190–206, <https://doi.org/10.1109/TGRS.2014.2320309>, 2014.
- Cardellach, E., Oliveras, S., Rius, A., Tomás, S., Ao, C. O., Franklin, G. W., Iijima, B. A., Kuang, D., Meehan, T. K., Padullés, R., de la Torre-Juárez, M., Turk, F. J., Hunt, D. C., Schreiner, W. S., Sokolovskiy, S. V., Van Hove, T., Weiss, J. P., Yoon, Y., Zeng, Z., Clapp, J., Xia-Serafino, W., and Cerezo, F.: Sensing heavy precipitation with GNSS polarimetric radio occultations, *Geophysical Research Letters*,  
645 46, 1024–1031, <https://doi.org/10.1029/2018GL080412>, 2019.
- Cazenave, Q., Ceccaldi, M., Delanoë, J., Pelon, J., Groß, S., and Heymsfield, A. J.: Evolution of DARDAR-CLOUD ice cloud retrievals: New parameters and impacts on the retrieved microphysical properties, *Atmospheric Measurement Techniques*, 12, 2819–2835, <https://doi.org/10.5194/amt-12-2819-2019>, 2019.
- Davis, C. P., Wu, D. L., Emde, C., Jiang, J. H., Cofield, R. E., and Harwood, R. S.: Cirrus induced polarization in 122 GHz aura Microwave  
650 Limb Sounder radiances, *Geophysical Research Letters*, 32, 1–4, <https://doi.org/10.1029/2005GL022681>, 2005.
- Defer, E., Galligani, V. S., Prigent, C., and Jimenez, C.: First observations of polarized scattering over ice clouds at close-to-millimeter wavelengths (157 GHz) with MADRAS on board the Megha-Tropiques mission, *Journal of Geophysical Research: Atmospheres*, 119, 12,301–12,316, <https://doi.org/10.1002/2014JD022353>, 2014.
- Delanoë, J. and Hogan, R. J.: A variational scheme for retrieving ice cloud properties from combined radar, lidar, and infrared radiometer,  
655 *Journal of Geophysical Research Atmospheres*, 113, 1–21, <https://doi.org/10.1029/2007JD009000>, 2008.
- Delanoë, J. and Hogan, R. J.: Combined CloudSat-CALIPSO-MODIS retrievals of the properties of ice clouds, *Journal of Geophysical Research*, 115, D00H29, <https://doi.org/10.1029/2009JD012346>, 2010.

- Draine, B. T. and Flatau, P. J.: Discrete-dipole approximation for scattering calculations, *Journal of the Optical Society of America A*, 11, 1491, <https://doi.org/10.1364/JOSAA.11.001491>, 1994.
- 660 Gong, J. and Wu, D. L.: Microphysical properties of frozen particles inferred from Global Precipitation Measurement (GPM) Microwave Imager (GMI) polarimetric measurements, *Atmospheric Chemistry and Physics*, 17, 2741–2757, <https://doi.org/10.5194/acp-17-2741-2017>, 2017.
- Gong, J., Zeng, X., Wu, D. L., and Li, X.: Diurnal Variation of Tropical Ice Cloud Microphysics: Evidence from Global Precipitation Measurement Microwave Imager Polarimetric Measurements, *Geophysical Research Letters*, 45, 1185–1193, 665 <https://doi.org/10.1002/2017GL075519>, 2018.
- Gong, J., Zeng, X., Wu, D. L., Munchak, S. J., Li, X., Kneifel, S., Liao, L., and Barahona, D.: Linkage among Ice Crystal Microphysics, Mesoscale Dynamics and Cloud and Precipitation Structures Revealed by Collocated Microwave Radiometer and Multi-frequency Radar Observations, *Atmospheric Chemistry and Physics*, 20, 12 633–12 653, <https://doi.org/10.5194/acp-20-12633-2020>, 2020.
- Hajj, G. A., Kursinski, E. R., Romans, L. J., Bertiger, W. I., and Leroy, S. S.: A Technical Description of Atmospheric Sounding By Gps 670 occultation, *Journal of Atmospheric and solar-terrestrial physics*, 64, 451–469, [https://doi.org/10.1016/S1364-6826\(01\)00114-6](https://doi.org/10.1016/S1364-6826(01)00114-6), 2002.
- Huang, L., Jiang, J. H., Wang, Z., Su, H., Deng, M., and Massie, S.: Climatology of cloud water content associated with different cloud types observed by A-Train satellites, *Journal of Geophysical Research: Atmospheres*, 120, 4196–4212, <https://doi.org/10.1002/2014JD022779>, 2015.
- Jameson, A. R.: Microphysical Interpretation of Multiparameter Radar Measurements in Rain. Part III: Interpretation and Measurement 675 of Propagation Differential Phase Shift between Orthogonal Linear Polarizations, *Journal of the Atmospheric Sciences*, 42, 607–614, [https://doi.org/10.1175/1520-0469\(1985\)042<0607:MIOMRM>2.0.CO;2](https://doi.org/10.1175/1520-0469(1985)042<0607:MIOMRM>2.0.CO;2), 1985.
- Janowiak, J., Joyce, B., and Xie, P.: NCEP/CPC L3 Half Hourly 4km Global (60S - 60N) Merged IR V1, Greenbelt, MD, Goddard Earth Sciences Data and Information Services Center (GES DISC), <https://doi.org/10.5067/P4HZB9N27EKU>, 2017.
- Kaur, I., Eriksson, P., Barlakas, V., Pfreundschuh, S., and Fox, S.: Fast Radiative Transfer Approximating Ice Hydrometeor Orientation and 680 Its Implication on IWP Retrievals, *Remote Sensing*, 14, 1–33, <https://doi.org/10.3390/rs14071594>, 2022.
- Kursinski, E. R., Hajj, G. A., Schofield, J. T., Linfield, R. P., and Hardy, K. R.: Observing Earth’s atmosphere with radio occultation measurements using the Global Positioning System, *Journal of Geophysical Research*, 102, 23 429–23 465, <https://doi.org/10.1029/97JD01569>, 1997.
- Leinonen, J. and Moisseev, D.: What do triple-frequency radar signatures reveal about aggregate snowflakes ?, *Journal of Geophysical 685 Research: Atmospheres*, 120, 229–239, <https://doi.org/10.1002/2014JD022072>, 2015.
- Liu, C. and Zipser, E. J.: The global distribution of largest, deepest, and most intense precipitation systems, *Geophysical Research Letters*, 42, 3591–3595, <https://doi.org/10.1002/2015GL063776>, 2015.
- Liu, G.: A Database of Microwave Single-Scattering Properties for Nonspherical Ice Particles, *Bulletin of the American Meteorological Society*, 89, 1563–1570, <https://doi.org/10.1175/2008BAMS2486.1>, 2008.
- 690 Mace, G. G., Protat, A., and Benson, S.: Mixed-Phase Clouds Over the Southern Ocean as Observed From Satellite and Surface Based Lidar and Radar, *Journal of Geophysical Research: Atmospheres*, 126, e2021JD034 569., <https://doi.org/10.1029/2021JD034569>, 2021.
- Marchand, R., Mace, G. G., Ackerman, T., and Stephens, G. L.: Hydrometeor detection using Cloudsat - An earth-orbiting 94-GHz cloud radar, *Journal of Atmospheric and Oceanic Technology*, 25, 519–533, <https://doi.org/10.1175/2007JTECHA1006.1>, 2008.
- Marshall, J., Donohoe, A., Ferreira, D., and McGee, D.: The ocean’s role in setting the mean position of the Inter-Tropical Convergence 695 Zone, *Climate Dynamics*, 42, 1967–1979, <https://doi.org/10.1007/s00382-013-1767-z>, 2014.

- Maxwell Garnett, J. C.: Colours in Metal Glasses and in Metallic Films, *Philosophical transactions of the Royal Society of London*, 203, 385–420, <https://doi.org/10.1098/rsta.1904.0024>, 1904.
- National Academies of Sciences Engineering and Medicine. : THRIVING ON OUR CHANGING PLANET A Decadal Strategy for Earth Observation from Space, <https://doi.org/10.17226/24938>., 2018.
- 700 Nguyen, C. M., Wolde, M., and Korolev, A. V.: Determination of Ice Water Content (IWC) in tropical convective clouds from X-band dual-polarization airborne radar, *Atmospheric Measurement Techniques*, 12, 5897–5911, <https://doi.org/10.5194/amt-12-5897-2019>, 2019.
- Oguchi, T.: Electromagnetic wave propagation and scattering in rain and other hydrometeors, *Proceedings of the IEEE*, 71, 1029–1078, <https://doi.org/10.1109/PROC.1983.12724>, 1983.
- 705 Padullés, R., Ao, C. O., Turk, F. J., de la Torre-Juárez, M., Iijima, B. A., Wang, K. N., and Cardellach, E.: Calibration and Validation of the Polarimetric Radio Occultation and Heavy Precipitation experiment Aboard the PAZ Satellite, *Atmospheric Measurement Techniques*, 13, 1299–1313, <https://doi.org/10.5194/amt-13-1299-2020>, 2020.
- Padullés, R., Cardellach, E., Turk, F. J., Ao, C. O., de la Torre-Juárez, M., Gong, J., and Wu, D. L.: Sensing Horizontally Oriented Frozen Particles With Polarimetric Radio Occultations Aboard PAZ: Validation Using GMI Coincident Observations and Cloudsat aPriori Information, *IEEE Transactions on Geoscience and Remote Sensing*, 60, 1–13, <https://doi.org/10.1109/TGRS.2021.3065119>, 2022.
- 710 Ryzhkov, A. V., Zrnić, D. S., and Gordon, B. A.: Polarimetric method for ice water content determination, *Journal of Applied meteorology*, 37, 125–134, [https://doi.org/10.1175/1520-0450\(1998\)037<0125:PMFIWC>2.0.CO;2](https://doi.org/10.1175/1520-0450(1998)037<0125:PMFIWC>2.0.CO;2), 1998.
- Ryzhkov, A. V., Pinsky, M., Pokrovsky, A., and Khain, A. P.: Polarimetric radar observation operator for a cloud model with spectral microphysics, *Journal of Applied Meteorology and Climatology*, 50, 873–894, <https://doi.org/10.1175/2010JAMC2363.1>, 2011.
- Schiro, K. A., Ahmed, F., Giangrande, S. E., and Neelin, J. D.: GoAmazon2014/5 campaign points to deep-inflow approach to deep convection across scales, *Proceedings of the National Academy of Sciences of the United States of America*, 115, 4577–4582, <https://doi.org/10.1073/pnas.1719842115>, 2018.
- 715 Schiro, K. A., Sullivan, S., Kuo, Y.-H., Su, H., Gentine, P., Elsaesser, G. S., Jiang, J. H., and Neelin, J. D.: Environmental Controls on Tropical Mesoscale Convective System Precipitation Intensity, *Journal of Atmospheric Sciences*, 77, 4233–4249, <https://doi.org/10.1175/JAS-D-20-0111.1>, 2020.
- 720 Schneider, T. L., Bischoff, T., and Haug, G. H.: Migrations and dynamics of the intertropical convergence zone., *Nature*, 513, 45–53, <https://doi.org/10.1038/nature13636>, 2014.
- Stephens, G. L., Vane, D. G., Tanelli, S., Im, E., Durden, S. L., Rokey, M., Reinke, D., Partain, P., Mace, G. G., Austin, R. T., L'Ecuyer, T., Haynes, J., Lebsock, M., Suzuki, K., Waliser, D. E., Wu, D. L., Kay, J., Gettelman, A., Wang, Z., and Marchand, R.: CloudSat mission: Performance and early science after the first year of operation, *Journal of Geophysical Research Atmospheres*, 113, 1–18, <https://doi.org/10.1029/2008JD009982>, 2008.
- 725 Storer, R. L. and Posselt, D. J.: Environmental impacts on the flux of mass through deep convection, *Quarterly Journal of the Royal Meteorological Society*, 145, 3832–3845, <https://doi.org/10.1002/qj.3669>, 2019.
- Turk, F. J., Padullés, R., Cardellach, E., Ao, C. O., Wang, K.-N., Morabito, D. D., de la Torre-Juárez, M., Oyola, M., Hristova-Veleva, S. M., and Neelin, J. D.: Interpretation of the Precipitation Structure Contained in Polarimetric Radio Occultation Profiles Using Passive Microwave Satellite Observations, *Journal of Atmospheric and Oceanic Technology*, 38, 1727–1745, <https://doi.org/10.1175/jtech-d-21-0044.1>, 2021.
- 730 Vivekanandan, J., Bringi, V. N., Hagen, M., and Meischner, P.: Polarimetric radar studies of atmospheric ice particles, *IEEE Transactions on Geoscience and Remote Sensing*, 32, 1–10, <https://doi.org/10.1109/36.285183>, 1994.



- 735 Wu, D. L., Austin, R. T., Deng, M., Durden, S. L., Heymsfield, A. J., Jiang, J. H., Lambert, A., Li, J. L., Livesey, N. J., McFarquhar, G. M.,  
Pittman, J. V., Stephens, G. L., Tanelli, S., Vane, D. G., and Waliser, D. E.: Comparisons of global cloud ice from MLS, CloudSat, and  
correlative data sets, *Journal of Geophysical Research: Atmospheres*, 114, 1–20, <https://doi.org/10.1029/2008JD009946>, 2009.
- Yurkin, M. A. and Hoekstra, A. G.: The discrete-dipole-approximation code ADDA: Capabilities and known limitations, *Journal of Quanti-  
tative Spectroscopy and Radiative Transfer*, 112, 2234–2247, <https://doi.org/10.1016/j.jqsrt.2011.01.031>, 2011.
- 740 Zeng, X., Skofronick-Jackson, G., Tian, L., Emory, A. E., Olson, W. S., and Kroodsma, R. A.: Analysis of the global microwave polarization  
data of clouds, *Journal of Climate*, 32, 3–13, <https://doi.org/10.1175/JCLI-D-18-0293.1>, 2019.